



Study on the energy evolution process and damage constitutive model of concrete–granite composite specimens under uniaxial compression load

Zhuo Dong · Yingxian Lang · Bin Gong ·
Ruifu Yuan · Zhengzhao Liang · Shanyong Wang ·
Chun'an Tang

Received: 23 June 2024 / Accepted: 24 November 2024
© The Author(s) 2024

Abstract The interaction between concrete structures and rock foundations is a crucial research topic for assessing safety and stability in geotechnical and underground engineering. The uniaxial compression tests were conducted on different combination modes (concrete component heights (H_c), interface inclination angle (β), and coarse aggregate contents) to investigate their impact on the mechanical and energy response of concrete–granite composite specimens (CGCSs). This study categorized three failure modes: only concrete component failure ($H_c=80$ mm), shear

failure along the interface ($\beta=30^\circ$), and simultaneous failure of both components (other combination modes). The fractal dimension (D_f) of surface cracks positively correlates with H_c , while the compressive strength (σ_{CGCS}) and stiffness (E_{CGCS}) exhibit an inverse trend. The value of D_f and σ_{CGCS} both exhibit a "U-shaped" trend when β ranges from 0° to 90° , whereas the value of E_{CGCS} decreases linearly. Moreover, The value of D_f and E_{CGCS} positively correlate with coarse aggregate contents, while the value of σ_{CGCS} trends vary non-monotonically increases. The coarse aggregate contents have few effects on energy conversion. Typical brittle failure ($\beta=0^\circ$, $\beta=30^\circ$, and $H_c=20$ mm) and ductile failure (other combination modes) are observed. Energy evolution characteristics offer quantitative insight into the damage evolution processes of CGCSs. The piecewise damage constitutive model based on dissipation energy can accurately describe the mechanical response of CGCSs. This study enhances understanding of the mechanical properties, failure characteristics, and energy evolution process of CGCSs under complex combination modes.

Z. Dong · R. Yuan
School of Energy Science and Engineering, Henan
Polytechnic University, Jiaozuo 454000, China

Z. Dong · R. Yuan
State Collaborative Innovation Center of Coal Work Safety
and Clean-Efficiency Utilization, Henan Polytechnic
University, Jiaozuo 454000, China

Y. Lang · Z. Liang · C. Tang
State Key Laboratory of Coastal and Offshore
Engineering, Dalian University of Technology,
Dalian 116024, Liaoning, China

B. Gong (✉)
Department of Civil and Environmental Engineering,
Brunel University London, London UB8 3PH, UK
e-mail: bin.gong@brunel.ac.uk

S. Wang
Discipline of Civil, Surveying and Environmental
Engineering, School of Engineering, The University
of Newcastle, Callaghan 2308, Australia

Highlights

- Uniaxial compression tests were conducted on the concrete–granite composite specimens with different combination modes.

- The mechanical properties and failure characteristics were observed.
- The energy evolution mechanism was investigated.
- A piecewise damage constitutive model was proposed.

Keywords Concrete–granite composite specimens · Uniaxial compression · Mechanical properties · Energy evolution process · Piecewise damage constitutive model

1 Introduction

Concrete–rock composite structures are prevalent in various engineering applications, including road and bridge engineering, tunneling, hydraulic engineering, and mining development (Son et al. 2013; Saichi et al. 2024; Yang et al. 2024; Yuan et al. 2024a, b; Zhao et al. 2019; Pereira et al. 2022; Qin et al. 2024). Concrete and rock possess different mechanical properties and failure modes, resulting in unique deformation and damage characteristics in composite specimens. Therefore, analyzing the interaction between the concrete and rock is essential to grasping composite specimens' failure modes and damage mechanisms.

Researchers have made significant progress in understanding the mechanical behaviors of composite specimens, covering compression (Selçuk et al. 2019; Yang et al. 2022), tensile properties (Wang et al. 2022; Li et al. 2022a, b, c; Zhou et al. 2022), shear failure of the interface (Lamber et al. 2010; Gutiérrez-Ch et al. 2018), and fracture mechanical properties (Yuan et al. 2024a, b; Lu et al. 2022; Chang et al. 2020). For instance, studies have focused on the mechanical properties and damage evaluation of composite specimens under complex stress conditions (Shen et al. 2022; Zhao et al. 2022). The interface inclination angle is also crucial in compressive mechanical properties and failure models (Selçuk et al. 2019; Gu et al. 2013). Meanwhile, the interface inclination angle significantly impacts the static and dynamic indirect behaviors of rock–concrete bi-material discs (Zhou et al. 2020). Studies are being conducted using direct tensile laboratory tests and numerical simulation to investigate the adhesion strength of rock–concrete specimens (Li et al. 2022a,

b, c). These studies have yielded meaningful results, laying the groundwork for subsequent research. However, applications in subgrade engineering, pile foundation structures, and underground space foundation engineering, among others, often involve the use of various construction techniques and geological factors. Therefore, conducting a comprehensive study on the influence of combination modes, which may have been overlooked in previous studies, is imperative to investigate the mechanical and failure properties of composite specimens under compression loads.

Additionally, existing research has primarily focused on mechanical parameters and failure characteristics (Yuan et al. 2024a, b; Yang et al. 2022; Li et al. 2022a, b, c; Yang et al. 2023) without considering the influence of combination modes on energy evolution. Macroscopic failure fundamentally involves the energy-driven process of damage evolution in rock and concrete materials (Du et al. 2023; Gong et al. 2023), wherein deformation and failure represent energy storage and release processes (Qin et al. 2024; Yang et al. 2023). Hence, researching the damage evolution mechanism of composite specimens from an energy perspective is crucial for understanding their mechanical properties.

Moreover, studying the energy exchange characteristics of composite specimens can effectively elucidate the damage evolution mechanism under specific external conditions, thus offering theoretical support for practical applications in concrete–rock structure engineering. Zhang et al. (2023) conducted cyclic shear tests on pre-heated sandstone–concrete interfaces to investigate energy degradation, providing valuable insights for studying mechanical degradation in deep underground engineering. Luan et al. (2024) investigated sandstone–shotcrete's mechanical behavior and energy dissipation under monotonic and cyclic triaxial loading, offering theoretical underpinnings for the subsequent establishment of damage models. Yuan et al. (2024a, b) integrated energy and damage theories to investigate the mechanical properties of sandstone–concrete composite bodies. Moreover, Zhao et al. (2023) studied the energy and damage evolution of mortar–sandstone specimens under impact load. These studies have significantly advanced the research of the mechanical properties of composite specimens and offer valuable guidance for practical engineering applications. However, a notable gap remains in research energy evolution

and damage processes under complex combination modes.

Previous studies have extensively focused on establishing various damage-constitutive models of rock materials (Zhang et al. 2024; Feng et al. 2024; Zheng et al. 2024). Statistical and energy methods have been proposed for compression damage constitutive models for hybrid fiber-reinforced concrete (Cui et al. 2020). Zhang et al. (2021a, b) established a statistical damage constitutive model for high-strength concrete under conventional triaxial compression based on energy dissipation density. Shen et al. (2022) proposed a damage constitutive model to illustrate the mechanical characteristics of concrete–rock composite under high temperature and uniaxial compression. However, the qualitative analysis of the four material parameters in this constitutive model was challenging. Notably, the compaction stage, resulting from the compaction of microcracks during the initial loading phase (Li et al. 2022a, b, c), was not adequately captured by the traditional constitutive model (Shen et al. 2022; Zhang et al. 2021a, b; Li et al. 2022a, b, c; Liu et al. 2021; Yu et al. 2024). Moreover, many studies have emphasized that material failure involves irreversible processes of energy absorption, storage, and release, underscoring the crucial role of energy evolution in the damage evolution mechanism of rock and concrete (Qin et al. 2024; Du et al. 2023; Liu et al. 2024; Gao et al. 2022; Gong et al. 2022). Given that the strength of concrete components is lower than rock components, the composite specimens' failure is similar to the concrete, featuring a pronounced initial compaction stage. Consequently, considering material failure characteristics and their relationship with energy evolution, it is necessary to propose a piecewise damage constitutive model for composite specimens, characterizing the compaction stage and subsequent stages of the stress–strain curve separately.

In conclusion, while numerous studies have examined the composite specimens' mechanical properties and failure characteristics under conventional combination mode, few have explored the relationship between the energy evolution process and damage formation characteristics or have only analyzed these properties separately. Moreover, there was limited research on mechanical, energy, and damage under the influence of interface

inclination angles (β), concrete component heights (H_c), and coarse aggregate contents. The uniaxial compression tests were conducted for different combination modes to address these issues. The fractal dimension of surface failure was quantitatively evaluated using 3D non-contact scanner technology and the box-counting dimension method. A piecewise damage constitutive model was established based on dissipation energy. Moreover, the stress state under different combination modes was also studied to theoretically illustrate the mechanics and failure mechanism of concrete–granite composite specimens (CGCSs).

2 Experiment program

2.1 Specimen

The CGCSs consist of granite and concrete components. Granite specimens were collected from Jining County, Shandong Province, China, ensuring consistency in experimental results by cutting all specimens from the same larger granite volume. Granite specimens were cut into cylindrical specimens (a height of 100 mm and a diameter of 50 mm) using diamond core bits. This cylindrical specimen was further cut into different types of granite components based on predetermined combination modes using a Linear Cutting Machine, as shown in Fig. 1a. The granite's uniaxial compressive strength and elastic modulus are 116.52 MPa and 22.73 GPa, respectively.

The concrete was prepared in the laboratory following the specification for mix proportion design of ordinary concrete: JGJ 55–2011 (2011). Ordinary Portland cement (OPC) (P.O42.5) was used as the cementitious material sourced from Henan Mengdian Group. The fine aggregate comprised natural river sand with a fineness modulus of 3.1 and particle sizes ranging from 2.5 to 4.3 mm. Hard gravel, continuously graded, was used as the coarse aggregate, ranging from 5.0 to 12.0 mm. Ordinary water was mixed, and fine and coarse aggregates were sourced from the building materials market in Jiaozuo County, Henan Province, China.

The granite interface was roughnessed to simulate the natural contact between the two components and positioned at the cylindrical mold bottom. Subsequently, mixed concrete was poured rapidly into the

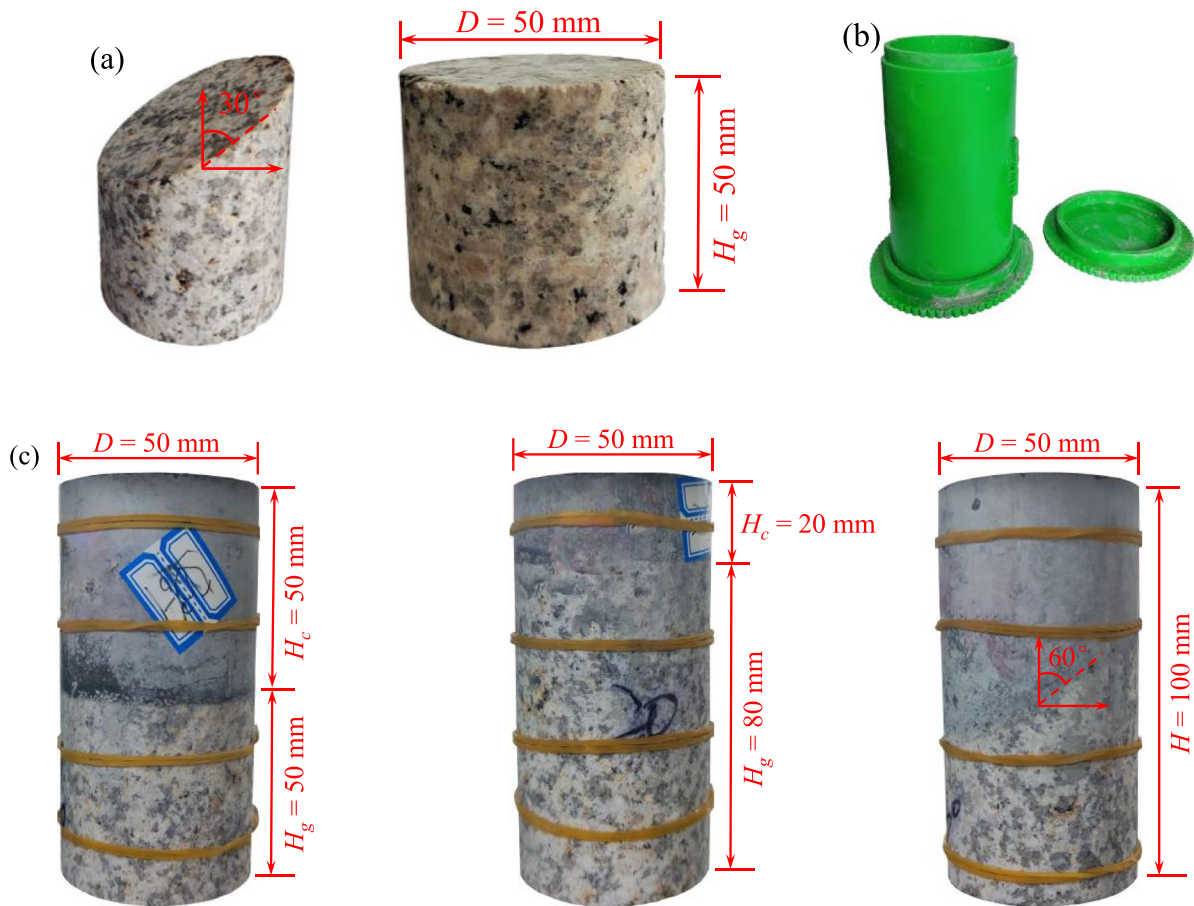


Fig. 1 CGCSs **a** pre-cutting granite components **b** cylindrical mold **c** different combination models of CGCSs

mold. A special vibrating device was then employed to vibrate the cast-in-place for approximately 2 min to ensure the high compactness of the concrete component. The CGCSs were left in the mold for 24 h and then cured in a Curing Standard Cabinet for 28 days at the standard curing temperature ($20 \pm 2 \text{ }^\circ\text{C}$ and 95%RH). The machining accuracy criteria for the specimens included non-parallelism between the ends face less than 0.1% of the diameter and a deviation between the end face and the axial direction not exceeding 0.25° .

The CGCSs with different combination modes are shown in Fig. 1c, including varying H_c , β , and coarse aggregate contents. The combination modes considered in this study have significant practical applications in foundation engineering, bridge foundations, tunnel lining support, and slope engineering. For instance, variations in support thickness or concrete strength grades are common in tunnel and underground space support engineering. Moreover, in slope, foundation, and dam engineering, the contact between concrete and inclined rock is prevalent, and

Table 1 Concrete–granite composite specimens

| Combination modes | Values/specimens number | | | | |
|---|-------------------------|------------|------------|------------|-------|
| Concrete component heights (H_c) | 20 mm | 40 mm | 50 mm | 60 mm | 80 mm |
| Interface inclination angle (β) | 0° | 30° | 60° | 90° | |
| Coarse aggregate contents | C-0 | C-1 | C-2 | C-3 | |

Table 2 Mixture properties of concrete component in CGCSs by weight ratio

| Specimens number | Cement | Water | Natural river sand | Hard gravel |
|------------------|--------|-------|--------------------|-------------|
| C-0 | 1 | 0.38 | 1.11 | 1.05 |
| C-1 | | | | 1.65 |
| C-2 | | | | 2.72 |
| C-3 | | | | 3.71 |

**Fig. 2** QKX-YD-1000 servo-controlled multifunctional rock loading system

the interface inclination angle plays a crucial role in sliding shear failure and overall structural stability. Through laboratory tests exploring different combination modes, the influence of mechanical and deformation behavior on structural stability and failure modes can be evaluated, which provides a theoretical foundation for engineering design.

A total of 40 CGCSs were prepared for tests and three sets of parallel tests for each combination mode, as shown in Table 1. The cement, water, natural river sand, and hard gravel have a weight ratio of 1: 0.38: 1.11: 2.72, used in different concrete component heights and interface inclination angles. Moreover, three different mixtures were designed to produce various strength concrete components, as shown in Table 2, with $H_c = 50$ mm and $\beta = 90^\circ$ (2011). The slump ranges are 100–130 mm (C-0), 70–100 mm (C-1), 50–70 mm (C-2), and 30–50 mm (C-3), respectively. C-0 and C-1 are classified as high-slump

concrete (70–150 mm), suitable for foundation or large-volume concrete that requires high fluidity but resists bleeding. C-2 and C-3 are medium-slump concrete (30–70 mm), suitable for conventional construction projects, ensuring sufficient flow and ease of construction. The concrete's uniaxial compressive strength and elastic modulus are 46.66 MPa and 18.87 GPa, respectively.

2.2 Experimental apparatus

Figure 2 displays the servo-controlled multifunctional rock loading system QKX-YD-1000 (for static and dynamic loading) utilized in this study at Henan Polytechnic University. This system comprises the support structure, hydraulic loading pump station, standard indenter (equipped with spherical seating), static sensor, and auxiliary system. The technical parameters of the loading system are as follows: maximum axial loading is 800 kN, maximum axial loading rate is 13 mm/s, and maximum axial displacement is 50 mm. Additionally, the accuracy of the deformation and stress measurement system is $\pm 1.0\%$, and the stiffness of the experimental device exceeds 8 GN/m. An axial LVDT is employed to obtain the axial displacement of the specimens and promptly feed back the measured data to the computer-control system.

To reduce the influence of the end friction between the specimen and the loading plate measures such as improving the specimen processing accuracy, using a spherical seating indenter, lubricating the specimen, and repeating tests were taken. During the test, 1.5 kN axial load was preloaded before the test to stabilize the specimen. Then axial displacement was applied at a loading rate of 0.0005 mm/s on contact with the concrete components until the specimen was destroyed.

Figure 3 depicts the OKIO-400 3D laser scanner, a collaborative development by Beijing Tianyuan 3D Technology CO., Ltd. and Tsinghua University. The main components include a computer-control system for data processing and display of the results, a grating emitter for transmission grating, two charge-coupled device cameras (CCD) for image capture, and a workbench. This device enables quick contactless scanning of objects, obtaining point cloud data of surface information, and generating a 3D data model after processing. Technical specifications of

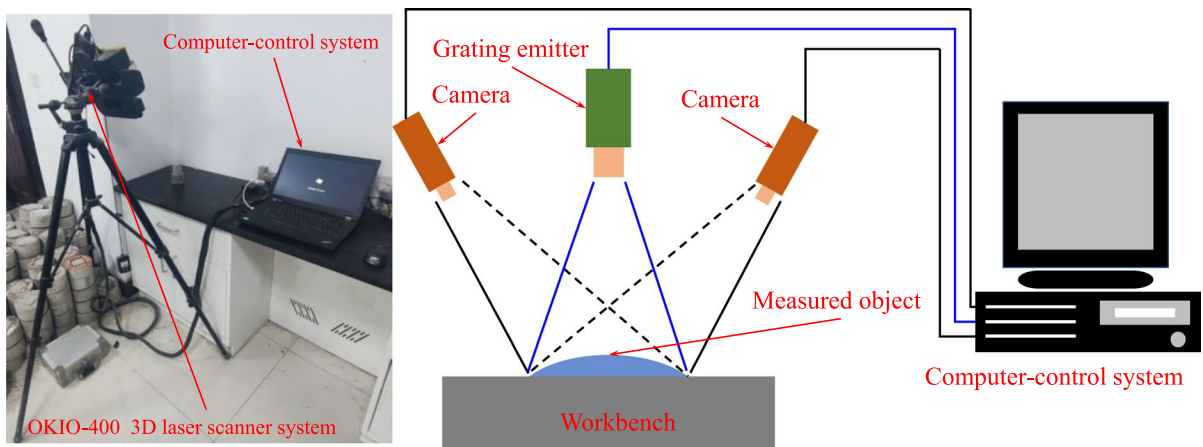


Fig. 3 OKIO-400 3D laser scanner system

the scanner device include a maximum scan coverage area of 400×300 mm, a single-face minimum measurement accuracy of 0.02 mm, and a high-precision industrial CCD with 480,000 pixels. Moreover, the system utilizes advanced structured light projection technology and heterodyne multi-frequency phase-shift 3D optical measurement technology, offering high measurement accuracy, fast speed, and strong anti-interference ability. During the measurement test, the grating emitter projects specially encoded structured light onto the object's surface, with the image captured simultaneously by two CCDs arranged at a certain angle. Subsequently, the image is decoded, and the phase is calculated to derive the 3D point cloud data of the object's surface.

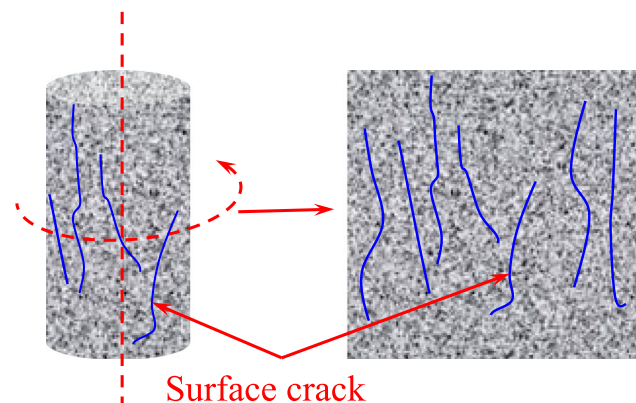
3 Results

3.1 Failure characteristics and mechanical properties

3.1.1 Failure characteristics

An OKIO-400 3D laser scanner was employed to scan the specimen surface from multiple angles, allowing for the automatic splicing of point cloud data to capture the three-dimensional surface crack characteristics. The open-source 3D point cloud and mesh processing software CloudCompare performed secondary point cloud data processing. This processing can expand the three-dimensional model along the specimen's height to derive the surface crack distribution under two-dimensional conditions, as illustrated in Fig. 4.

Fig. 4 Specimen expand



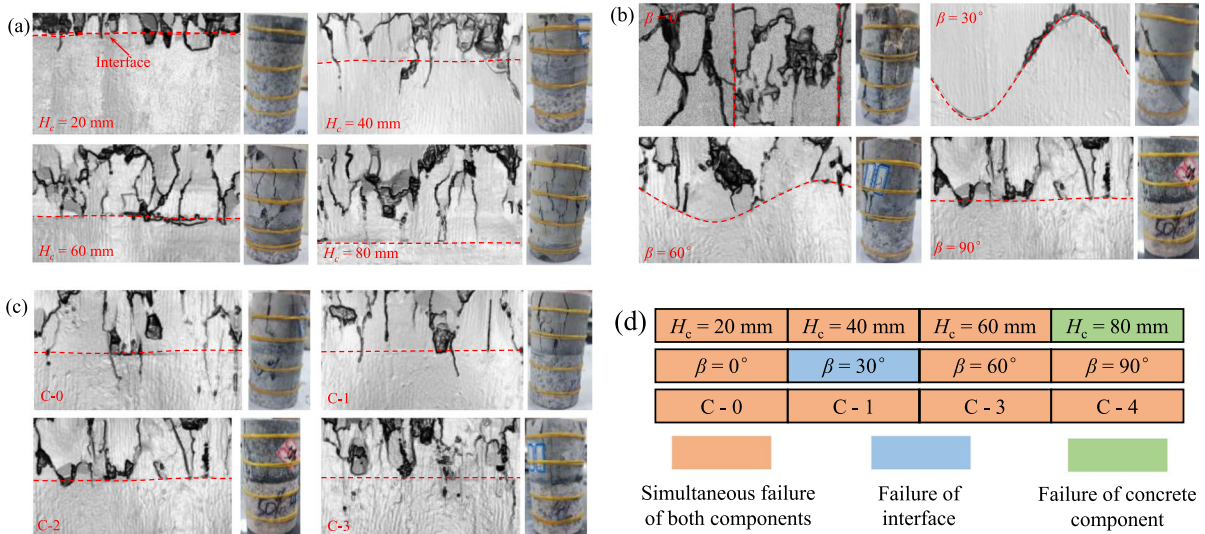


Fig. 5 Failure characteristics **a** concrete component heights **b** interface inclination angles **c** coarse aggregate contents **d** failure modes

The failure characteristics of CGCSs with different combination modes are depicted in Fig. 5. The failure is predominantly concentrated in the concrete components. This occurrence can be attributed to the granite’s higher strength than the concrete. As illustrated in Fig. 5a, significant crack propagation and typical spalling failure (darker areas) can be observed in the concrete components. Many failures are observed on the concrete component surface, while the granite component exhibits fewer cracks. Due to the significant disparity in the mechanical properties between the granite and concrete, the failure characteristics of CGCSs differ substantially from those of the concrete and granite specimens (Dong et al. 2024). The lower strength of concrete compared to granite means that the energy released upon concrete component failure during uniaxial compression further contributes to the failure of granite components. Considering the inherent heterogeneity of the two components and the presence of an interface, the energy distribution at the interface becomes uneven. Consequently, some macro-cracks formed in concrete components propagate to granite components, while others are arrested at the interface due to a lesser amount of driving energy. These results highlight the significant impact of the interface on crack propagation and its potential role in arresting crack growth. When $H_c = 40\text{ mm}$,

the failure characteristics closely resemble those observed with 20 mm.

Under $H_c = 60\text{ mm}$, only minimal failure occurs in the granite component near the interface, with no macroscopic cracks forming. The loss of bearing capacity in CGCSs is primarily attributed to the failure of concrete components. When $H_c = 80\text{ mm}$, macroscopic cracks predominately emerge in the concrete components, while no damage occurs in the granite component. Moreover, as the concrete component height increases, significant volume expansion is observed within the concrete component, indicating greater radial deformation. Numerous macroscopic cracks parallel to the loading direction are observed in the concrete components. Concrete is commonly conceptualized as a three-phase material consisting of coarse aggregate, mortar matrix, and interfacial transition zone (ITZ) between them. Hence, the formation of secondary cracks with varied shapes within concrete components is affected by different factors, such as aggregate shape, size, distribution position, and ITZ.

The failure characteristics under different concrete component heights can also be explained from the perspective of energy evolution. As shown in Fig. 5a, when the concrete component height exceeds 50 mm, the energy provided by the external load is entirely consumed by concrete components. Hence,

macroscopic cracks rarely form in the granite components. However, when the concrete component height is less than 50 mm, the energy provided by the external load cannot be fully consumed by the concrete component failure. As a result, a small amount of damage is formed in the granite components to consume the remaining energy.

The interface's strength is the lowest under the current specimen production conditions. When $\beta=0^\circ$, failure initially forms along the interface, separating the concrete and granite components and exhibiting a "parallel" mode, as shown in Fig. 5b. The CGCSs display failure characteristics of a two-body two-medium model, wherein both components lose their bearing capacity during loading processes. The concrete component fails first due to its weaker strength, while the granite component can continue to bear part of the external load until it becomes unstable. Due to the difference in elastic modulus between the concrete and granite components, the axial and radial deformation in CGCSs is not coordinated. Additionally, a typical axial splitting failure is observed along the loading direction in the granite components, with the upper part exhibiting a higher degree of failure. With a significant amount of energy released by the granite component, secondary failure occurs in the concrete component, resulting in severe failure in CGCSs. Furthermore, a typical spalling failure of mortar can be observed in the middle part of concrete components.

As the interface inclination angle increases, the CGCSs transition from the "parallel" mode to the "series" mode and exhibit a one-body two-medium model. When $\beta=30^\circ$, shear-induced cracks were observed along the interface. The lack of deformation coordination at the interface leads to small failures in the concrete components near the interface, while no damage occurs in the granite components. When $\beta=60^\circ$, failure primarily occurs in the concrete component, indicating that the influence of the weakest interface on its failure characteristics decreases, and it is primarily controlled by the concrete components. Almost no failure was observed in the granite component. Under $\beta=90^\circ$ and $H_c=50$ mm, the failure characteristics are similar to 60° .

As depicted in Fig. 5a, b, the failure characteristics of CGCSs are primarily determined by concrete components. Hence, it becomes imperative to investigate the mechanical behaviors of CGCSs under varying aggregate contents. Figure 5c illustrates the failure

characteristics under various coarse aggregate contents. The failure occurs in both concrete and granite components, with the failure degree of the concrete component surpassing that of the granite component. The mortar spalling failure becomes more significant with an increase in coarse aggregate contents. Furthermore, the presence of coarse aggregate leads to cracks in concrete components propagating in two ways, terminating the aggregate or bypassing it. Therefore, the increase in aggregate content can impede crack growth while it increases the area of ITZ, resulting in a more tortuous crack path characterized by a severe damage degree.

The failure characteristics of CGCSs with different combination modes under uniaxial compressive load reveal three distinct failure modes: only concrete component failure ($H_c=80$ mm), shear failure along the interface ($\beta=30^\circ$), and simultaneous failure of both components (other combination modes), as shown in Fig. 5d.

The fractal dimension serves as a tool to quantify the complexity and irregularity of shapes, making it particularly useful in analyzing the failure of rock materials. The box-counting dimension method stands out for its ability to directly capture the distribution deformation in failure images, and its intuitive calculation process has made it widely adopted in fractal analysis. The Moments algorithm, known for its effectiveness in image processing, is employed in this study. Utilizing ImageJ image processing software, the original grayscale image is binarized and denoised to obtain a refined distribution of surface cracks, as depicted in Fig. 6b, where the black pixels represent cracks or damaged areas in the failure image.

Figure 6c illustrates the box-counting dimension method. A rectangular grid (boxes) characterized by a side length (r) overlays the failure image (Fig. 6b), and the count is made of the number of rectangular grids (N_r) containing cracks and damage. Subsequently, the side length of the box is halved iteratively until its value approaches 0 while counting the number of rectangular grids (N_{r_i}) within the designated area. The natural logarithm of the side length (r_i) and the corresponding count of rectangular grid number (N_{r_i}) are then computed. Regression analysis of this statistical data is conducted using the least square method in the double logarithmic coordinate system facilitated by MATLAB. If the failure exhibits clear fractal characteristics, the statistical data conforms to the linear relationship outlined

in Eq. (1). The slope of Eq. (1) yields the fractal dimension and can be expressed as Eq. (2) (Xiao et al. 2024).

$$\lg N(r) = D_f \lg r + b \tag{1}$$

$$D_f = -\lim_{r \rightarrow 0} \frac{\lg(N(r))}{\lg(r)} \tag{2}$$

where r is the box's side length, $N(r)$ is the number of rectangular grids containing failure information, D_f is the fractal dimension.

The complexity of a failure image correlates positively with its fractal dimension. Figure 7 shows the fitting lines of box-dimension under different combination models. The fitting coefficients R^2 all approach 0.99, indicating that the failure characteristics of surface cracks in CGCSs conform to the fractal law. In Fig. 7a, d, it can be found that the fractal dimension (D_f) positively correlates with the concrete component heights. These results indicate that the more concrete component percentages, the more severe the failure degree of CGCSs. This is attributed to failure predominately occurring with the concrete components, as illustrated in Fig. 5a.

When β ranges from 0° to 90° , as shown in Fig. 7b, d, The fractal dimension (D_f) initially decreases and

then increases trend. Due to more significant energy release and leading to severe crushing, the highest fractal dimension is obtained at $\beta=0^\circ$. Conversely, when $\beta=30^\circ$, a simple failure mode (shear failure along the interface) occurs in CGCSs, resulting in the smallest fractal dimension. Moreover, as shown in Fig. 7c, d, the fractal dimension (D_f) positively correlates with the coarse aggregate content, indicating that damage tends to be severe. Therefore, particular attention should be given to concrete component height and interface inclination angle in practical engineering, optimizing the coarse aggregate content and then obtaining excellent mechanical properties of CGCSs.

3.1.2 Compressive strength and stiffness

The compressive strength (σ_{CGCS}) and stiffness (E_{CGCS}) under different combination modes are shown in Table 3 and Fig. 8. As presented in Fig. 8a, the value of σ_{CGCS} notably decreases when H_c ranges from 20 to 50 mm, and then remains almost constant as the concrete component height continue increases. The value of σ_{CGCS} is influenced by both the two components and is closely tied to the height ratio of these components (Dong et al. 2024). With

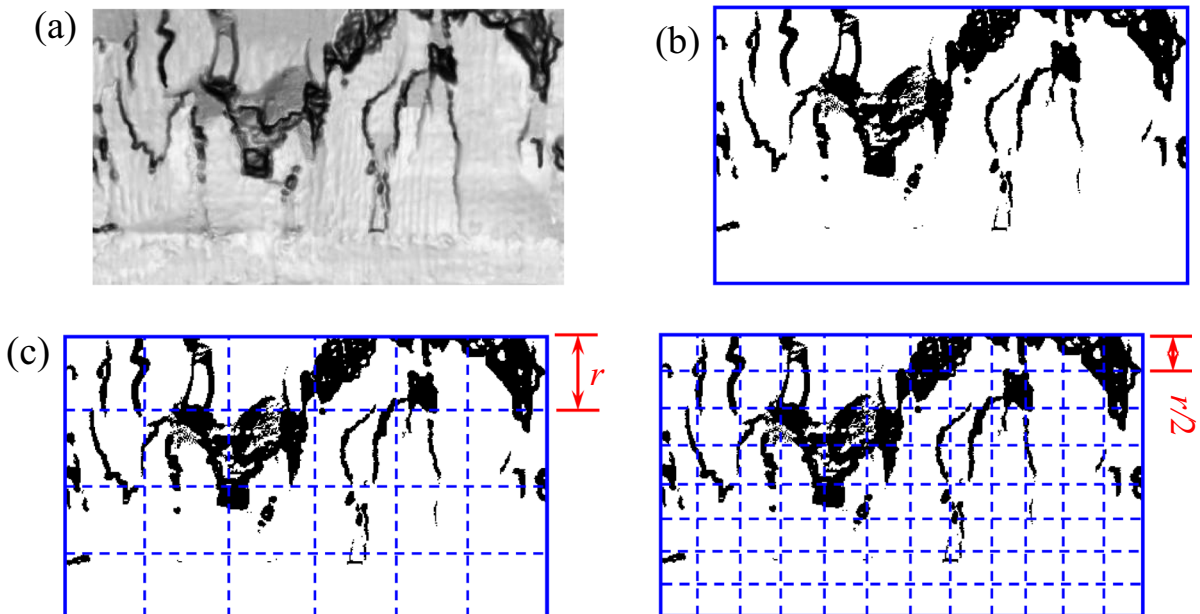


Fig. 6 The processing of failure image and box-counting method **a** grayscale image **b** binarization and denoise **c** box-counting method

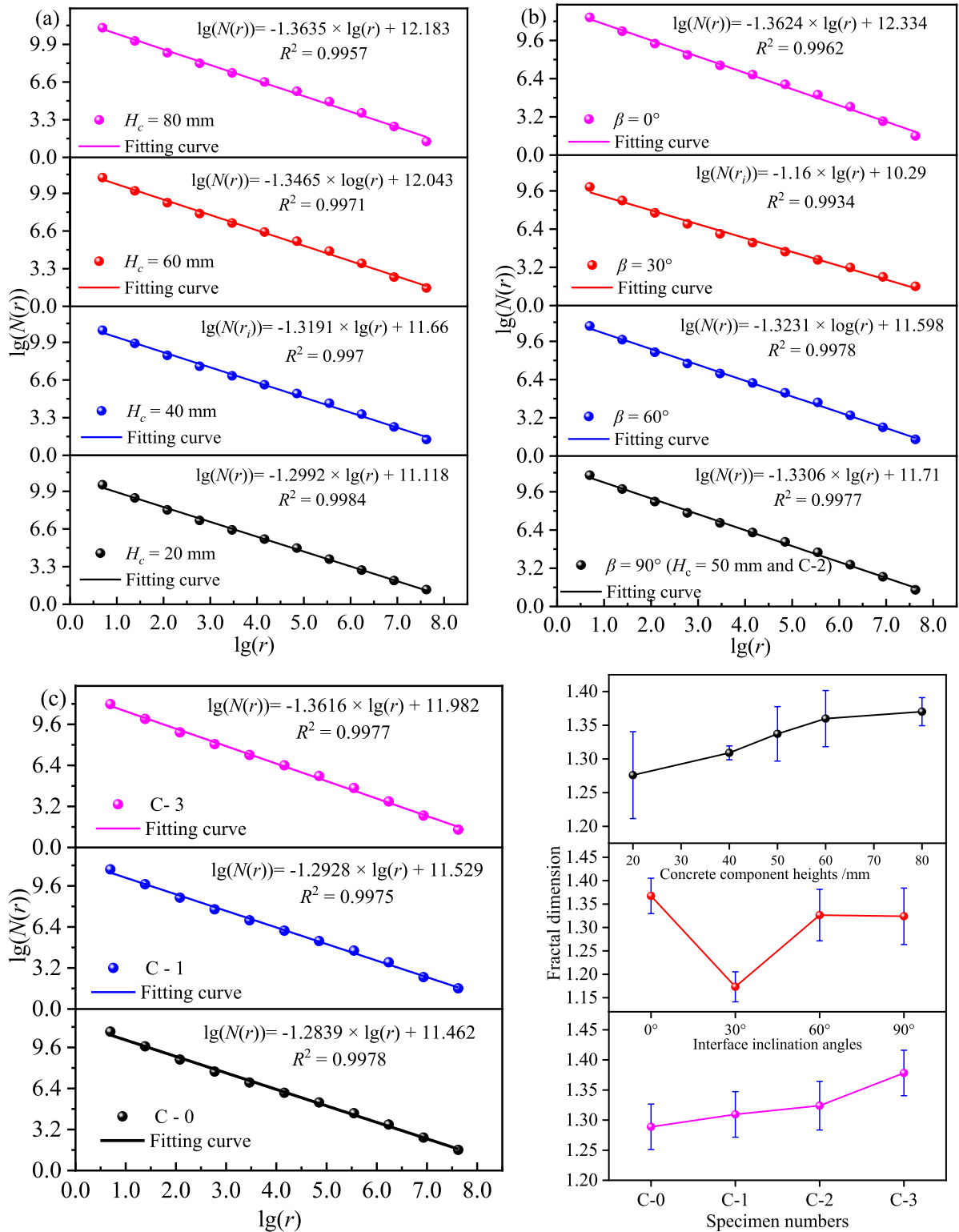


Fig. 7 Relationship between $\lg N(r)$ and $\lg(r)$ of surface crack **a** concrete component heights **b** interface inclination angles **c** coarse aggregate contents **d** change of fractal dimension

Table 3 Compression strength and stiffness under different combination modes

| Specimens | | Compression strength (MPa) | | | Stiffness (GPa) | | |
|-------------------------------|-----|----------------------------|-------|-------|-----------------|-------|-------|
| Concrete component height /mm | 20 | 85.40 | 90.09 | 85.06 | 18.89 | 23.56 | 22.50 |
| | 40 | 60.10 | 61.42 | 63.67 | 22.34 | 19.52 | 20.42 |
| | 50 | 47.36 | 53.26 | 47.16 | 21.96 | 18.56 | 17.59 |
| | 60 | 46.25 | 50.18 | 45.77 | 19.56 | 18.28 | 19.79 |
| | 80 | 45.18 | 51.26 | 46.72 | 15.28 | 18.79 | 17.92 |
| Interface inclination angle | 0° | 73.26 | 78.25 | 76.01 | 20.29 | 23.89 | 19.99 |
| | 30° | 35.21 | 37.82 | 38.18 | 19.89 | 22.56 | 19.56 |
| | 60° | 50.23 | 51.36 | 44.57 | 19.05 | 22.35 | 22.35 |
| | 90° | 47.36 | 53.26 | 47.16 | 21.96 | 18.56 | 17.59 |
| Coarse aggregate contents | C-0 | 46.25 | 49.86 | 47.44 | 17.25 | 19.63 | 18.11 |
| | C-1 | 51.21 | 51.36 | 56.10 | 18.75 | 20.01 | 17.55 |
| | C-2 | 47.36 | 53.26 | 47.16 | 21.96 | 18.56 | 17.59 |
| | C-3 | 54.21 | 57.36 | 54.75 | 18.56 | 21.05 | 22.88 |

an increase in concrete component height, the contribution of concrete components to the value of σ_{CGCS} gradually increases, while the contribution of granite components gradually decreases. Due to concrete's lower strength than granite, the value of σ_{CGCS} exhibits a gradual decreasing trend. Specifically, the compressive strength of concrete is 46.66 MPa. When the concrete component height exceeds 50 mm, the value of σ_{CGCS} is nearly equal to that of the concrete specimen, indicating that the concrete component predominantly determines the value of σ_{CGCS} . The above results are linked to the failure mode of CGCSs and the disparity in strength between the two components (the failure mode was discussed in detail in Sect. 3.1.1).

Additionally, as shown in Fig. 8a, the value of E_{CGCS} decreases with an increase in concrete component heights, indicating a gradual decrease in the stiffness of CGCSs. The value of E_{CGCS} ranges only from 21.65 to 17.33 GPa, with a maximum reduction rate of 19.95%. However, the values of σ_{CGCS} range from 86.85 to 47.47 MPa, with a maximum reduction rate of up to 45.34%. The results indicate that the impact of concrete component height on compressive strength is greater than that on stiffness.

Figure 8b shows the mechanical properties under various interface inclination angles. The value of σ_{CGCS} noticeably decreases as β ranges from 0° to 30°, with a reduction rate of 51.12%. Subsequently, its values demonstrated gradually increasing trends for interface inclination angles larger than 30°.

Meanwhile, in comparison with $\beta=0^\circ$, the compressive strength falls by 35.76% and 35.05% when β ranges from 60° to 90°. This indicates a significant influence of the interface inclination angles on the value of σ_{CGCS} under a small angle, while this influence diminishes as the interface inclination angle increases. The results can be attributed to the differing relative position of the two components. For $\beta=0^\circ$, the CGCSs exhibit a "parallel" model, and their strength is shared by both components. When the concrete component is damaged, the granite component, with higher strength, retains some bearing capacity until it is also compromised. Hence, the maximum σ_{CGCS} value is determined by both the two components ($\beta=0^\circ$), with the concrete component exerting a controlling influence. Conversely, a shear failure along the interface occurs at $\beta=30^\circ$, and the value of σ_{CGCS} is dictated by the shear strength of the interface, leading to the specimens exhibiting the minimal value of σ_{CGCS} . Similar to the strength anisotropy observed in layered rocks (such as shale and sandstone) (Heng et al. 2015), the relationship between the value of σ_{CGCS} and the interface inclination angles shown in Fig. 8b exhibits a "U-shaped" trend.

Moreover, the value of σ_{CGCS} remains almost constant when β ranges from 60° to 90°. This can be explained as CGCSs adopting a "series" model, with failure primarily occurring in the concrete components. Although the granite component contributes somewhat to the compressive strength of

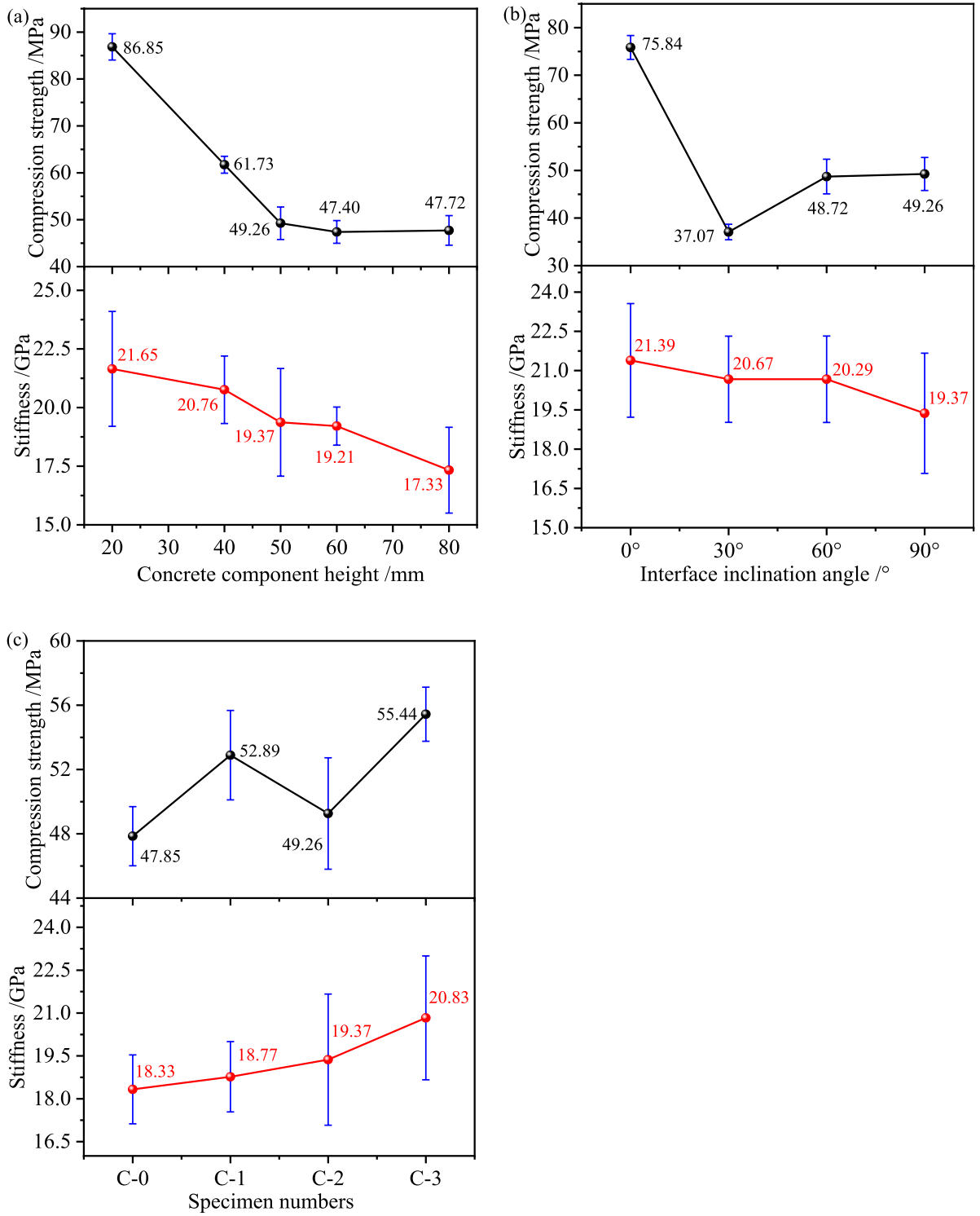


Fig. 8 The compressive strength and stiffness **a** concrete component height **b** interface inclination angle **c** coarse aggregate contents

CGCSs, its influence is minimal. The compressive strength of CGCSs is predominantly controlled by the concrete component. Consequently, the values of σ_{CGCS} are nearly equivalent to the strength of concrete specimens.

Additionally, as illustrated in Fig. 8b, the value of E_{CGCS} decreases linearly with increasing interface inclination angle. In comparison with $\beta=0^\circ$, the value of E_{CGCS} decreases by 3.36%, 5.14%, and 9.47% when β ranges from 30° to 90° . This indicates that the interface inclination angle has minimal effects on the stiffness of CGCSs. Therefore, considering the difficulty in ensuring complete horizontal alignment of the contact surface between concrete and rock in practical engineering, it is crucial to account for the influence of interface inclination angle to explore the mechanical properties of CGCSs.

Figure 8c illustrates the mechanical properties under different coarse aggregate contents. The value of E_{CGCS} increases linearly with increasing coarse aggregate content. In comparison with C-0, the value of E_{CGCS} increases by 2.4%, 5.67%, and 13.64% respectively for C-1, C-2, and C-3. This indicates that coarse aggregate contents also have minimal effects on the stiffness. The high strength of coarse aggregate itself can bear a portion of the external load and hinder further crack propagation, positively impacting the concrete strength. However, the augmentation in coarse aggregate contents increases the interface transition zone (ITZ). The weak strength of ITZ facilitates crack propagation and negatively affects the concrete strength. The interaction mechanism between the coarse aggregate and ITZ is relatively complex. Moreover, the weaker concrete components determine the overall strength of CGCSs (Dong et al. 2024). Consequently, as shown in Fig. 8c, the influence of coarse aggregate contents on the value of σ_{CGCS} is not monotonically increasing. Additionally, for the C-2 specimen, the coarse aggregate change caused a significant negative impact on the strength of concrete components, resulting in a decrease in the value of σ_{CGCS} .

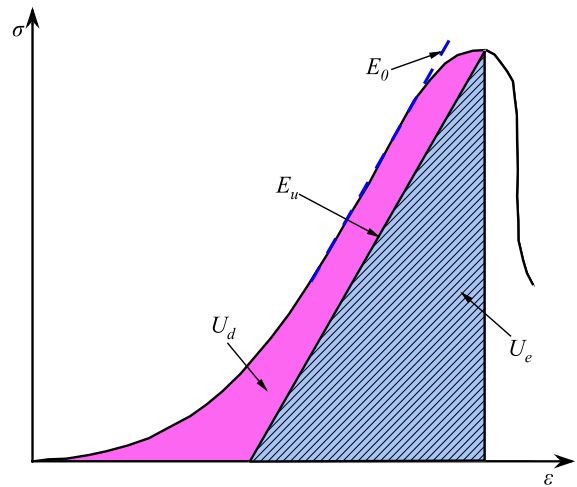


Fig. 9 Energy conversion under uniaxial loading conditions

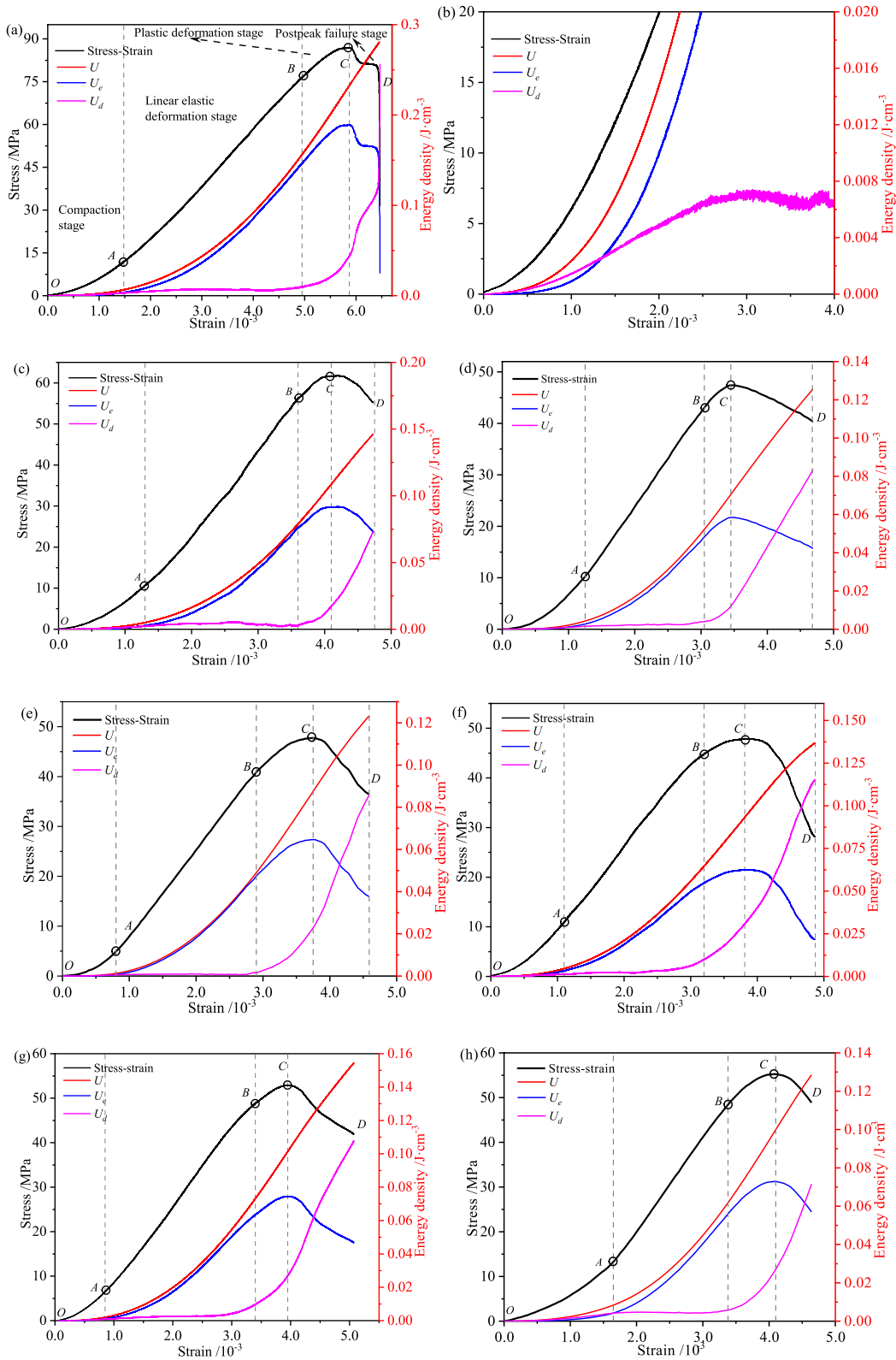
3.2 Energy evolution

3.2.1 Principle of energy calculation

The CGCSs undergo a process from local failure to global instability failure under external load, constituting an irreversible energy conversion process accompanied by energy absorption, dissipation, and release (Gong et al. 2023). This highlights the critical role of energy evolution during the damage of CGCSs (Du et al. 2023; Qin et al. 2024). According to the first law of thermodynamics, and without considering external temperature change or material exchange during testing, the total energy injected (U) into the specimen by the external loading system can be divided into two components: elastic energy (U_e) and dissipation energy (U_d), as shown in Fig. 9. The dissipation energy primarily encompasses surface energy consumed during fracture and pores generation, extension, and expansion, plastic energy during irreversible plastic deformation of concrete, and the heat generated by friction between fractures. This constitutes an irreversible energy conversion process, resulting in damage occurring in CGCSs.

Therefore, the energy conversion during the deformation and damage process can be expressed by Eq. (3) (Solecki et al. 2003; Qin et al. 2024; Du et al. 2023).

$$U = U_e + U_d \tag{3}$$



◀**Fig. 10** Energy evolution process **a** $H_c=20$ mm **b** local amplification for $H_c=20$ mm **c** $H_c=40$ mm **d** $H_c=60$ mm **e** $H_c=80$ mm **f** C-0 **g** C-1 **h** C-3

where U , U_e , and U_d are the total energy (J/cm^3), the elastic energy (J/cm^3), and the dissipation energy (J/cm^3), respectively.

Under triaxial loading conditions, the energy relationship of each unit can be calculated using Eqs. (4) and (5), as shown in the following (Solecki et al. 2003; Luo et al. 2022):

$$U = \int_0^{\epsilon_1} \sigma_1 d\epsilon_1 + \int_0^{\epsilon_2} \sigma_2 d\epsilon_2 + \int_0^{\epsilon_3} \sigma_3 d\epsilon_3 \tag{4}$$

$$U_e = \frac{1}{2E_u} [\sigma_1^2 + \sigma_2^2 + \sigma_3^2 - 2\bar{\mu}(\sigma_1\sigma_2 + \sigma_2\sigma_3 + \sigma_1\sigma_3)] \tag{5}$$

where σ_1 , σ_2 , and σ_3 are the maximum, intermediate, and minimum principal stresses, respectively. ϵ_1 , ϵ_2 , and ϵ_3 are the elastic strains of specimens corresponding to σ_1 , σ_2 , and σ_3 , respectively. E_u is the unloading elastic modulus and $\bar{\mu}$ is the unloading Poisson’s ratio.

Under uniaxial compression loading conditions ($\sigma_2=\sigma_3=0$), the elastic energy consists of the axial and circumferential energy, and the circumferential energy is much smaller than the axial energy. Hence, the influence of circumferential energy can usually be ignored. Meanwhile, the initial elastic modulus (E_0) and Poisson’s ratio (μ) obtained from the linear stage of the stress–strain curve are used instead of the unloading elastic modulus and unloading Poisson’s ratio to calculate the energy. Therefore, the U , U_e , and U_d values under uniaxial loading conditions can be calculated using Eqs. (6)–(8), as shown in the following (Solecki et al. 2003):

$$U = \int_0^{\epsilon_1} \sigma_1 d\epsilon_1 \tag{6}$$

$$U_e = \frac{1}{2E_0} \sigma_1^2 \tag{7}$$

$$U_d = \int_0^{\epsilon_1} \sigma_1 d\epsilon_1 - \frac{1}{2E_0} \sigma_1^2 \tag{8}$$

3.2.2 Energy evolution process

The energy evolution of CGCSs uniaxial compression loading conditions can be obtained from Eqs. (6)–(8). Figure 10 shows the energy evolution process under different concrete component heights and coarse aggregate contents. It can be observed that the pre-peak plastic deformation has similar stage characteristics under different combination modes. The damage deformation process can be divided into four stages: compaction (OA), linear elastic deformation (AB), plastic deformation (BC), and post-peak failure (CD). Taking $H_c=20$ mm as an example, the four stages are characteristics:

(1) Compaction stage (OA): During the initial loading stage, the original microcracks and pores structure inside the specimen gradually close, and the specimen is compacted, forming an early nonlinear deformation, and the stress–strain curve exhibits an upper concave type. Meanwhile, the value of U and U_e increase nonlinearly with deformation, and the value of U_d increases in a flat ‘‘S-shaped’’. Figure 10b presents the local amplification of the energy evolution at the compaction stage. When the axial strain is smaller than 1.34×10^{-3} , the value of U_d is larger than U_e , the reason can be explained as most energy was consumed by microcracks closure and friction in the specimen. However, with the increase of deformation and microcracks closure, the effective contact area inside the specimen increases, and the accumulation rate of elastic energy increases while the accumulation rate of dissipation energy decreases. When the curves of U_e and U_d cross, the growth rate of elastic energy is gradually greater than that of dissipation energy, and it is consistent with the growth rate of total energy input by the loading system.

(2) Linear elastic deformation stage (AB): The value of U and U_e increase linearly with deformation, while the value of U_d remains relatively lower and is almost unchanged. The microcracks and pores inside the specimen are completely closed, and the value of U input by the loading system is mainly converted into U_e and stored inside the specimen. This indicates that the specimen accumulates recoverable elastic deformation with continuous loading at this stage and only a relatively small amount of micro-damage forms in the specimen.

(3) Plastic deformation stage (BC): Under the continuous loading, the initiation, propagation, and interpenetration of cracks will consume part of the value

of U , accompanied by irreversible plastic deformation and other different forms of energy consumption. Therefore, the value of U and U_e continue to increase

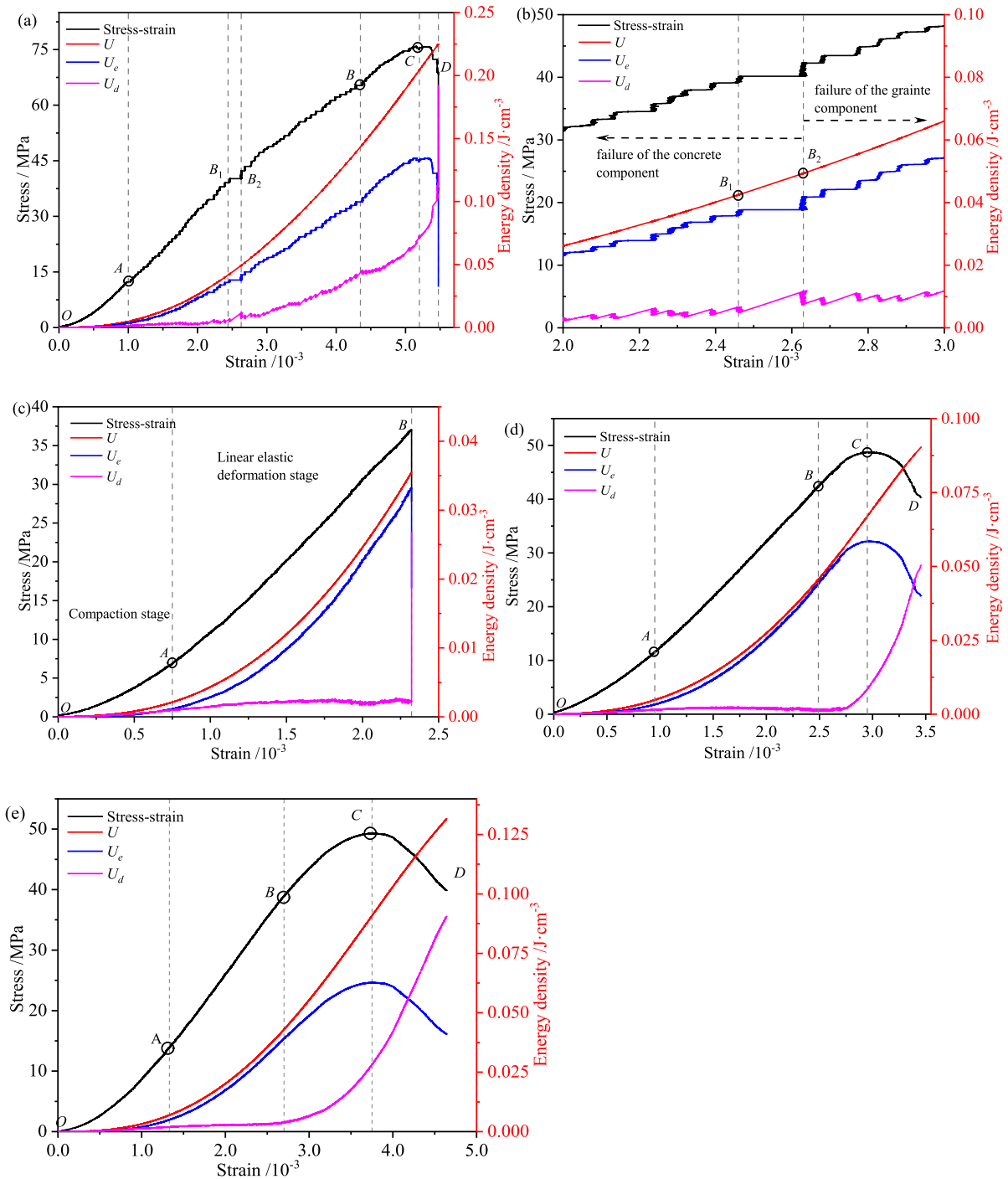


Fig. 11 Energy evolution process **a** $\beta=0^\circ$ **b** local amplification for $\beta=0^\circ$ **c** $\beta=30^\circ$ **d** $\beta=60^\circ$ **e** $\beta=90^\circ$ ($H_c=50$ mm and C-2)

with deformation. At the same time, the growth rate of elastic energy gradually decreases and reaches the maximum value at peak stress (energy storage limit). The value of U_d shows an increasing trend, and its growth rate increased gradually.

Under the influence of concrete component heights and coarse aggregate contents, the stress–strain variation trends before peak stress are similar to each other. However, there is a significant difference during the post-peak stress stage.

(4) Post-peak failure stage (CD): When $H_c = 20$ mm, although failure still primarily occurs in the concrete component, the post-peak stage is shorter due to the lower concrete component height. After a small degree of ductile failure, it shows a typical brittle failure, which is similar to the granite specimen. With an increase in concrete component heights, ductile failure occurs in CGCSs, as shown in Fig. 11c–h.

Combined with Fig. 6a and c, the failure is primarily concentrated in the concrete components, leading to the ductile failure characteristics being similar to concrete (Liu et al. 2021). Additionally, the elastic energy is released in a short time when $H_c = 20$ mm, and the value of U_d increases rapidly, indicating that a larger number of microcracks in the specimen are connected to form macroscopic cracks. Finally, this leads to the complete failure of CGCSs.

The above results indicate that the total energy is primarily stored in the specimen in the elastic energy form under the pre-peak stage, which is the energy source of failure after the peak stress. Moreover, other forms of energy dissipation during the pre-peak stage reduce the specimen's bearing ability. During the post-peak stage, the elastic energy is released, and the proportion of dissipation energy in the total energy increases.

Figure 11 shows the energy evolution process for various interface inclination angles. Under $\beta = 60^\circ$ and $\beta = 90^\circ$, simultaneous failure of both components is formed and concentrated in the concrete components, indicating that the stress–strain and energy evolution regularities are similar to those under different coarse aggregate contents. Meanwhile, the stress–strain regularities under $\beta = 0^\circ$ are generally similar to $H_c = 20$ mm. However, due to the special relative positions of the two components under $\beta = 0^\circ$, the failure process is significantly different from that of $H_c = 20$ mm, resulting in different energy evolution processes. The failure first forms in the concrete

component with weaker strength, and with the continuous loading, the granite component gradually causes damage, finally leading to the overall instability of CGCSs. Therefore, a typical compaction stage (OA) occurs at the beginning of loading, as shown in Fig. 11a. Then both the two components bear the external load and enter the linear deformation stage.

As shown in Fig. 11a, the value of U and U_e increase, while the value of U_d remains unchanged during the AB_1 stage. Due to the failure first forms in the concrete components with a lower strength, the granite component can continue to bear part of the external load, the stress shows constant as the strain increases (B_1B_2). During the B_1B_2 stage, the value of U continues to rise, the value of U_e remains unchanged, and the value of U_d appears to have a small increase trend, an important mark of the damage in the concrete components. Under continuous loading, the control effect of granite components is enhanced, and the stress increases with the increase of strain. The value of U and U_e are gradually increased, and the difference between them increases. The value of U_d shows an increasing trend. The reason can be explained as the continuous failure of concrete components and the internal damage development of granite components to consume part of the input energy. The growth rate of elastic energy decreases while the growth rate of dissipation energy increases, and the specimen enters the elastic deformation stage. When the peak strength is reached, the value of U_d increases rapidly and exhibits typical brittle failure characteristics. Moreover, as a typical brittle material, the dissipation energy of granite is much higher than concrete.

When $\beta = 30^\circ$, shear failure along the interface is formed, and no obvious damage is found in the two components. Therefore, the deformation and energy show different trends. The compaction phenomenon occurs in the initial stage and then enters the linear elastic deformation stage. No plastic deformation stage forms during the pre-peak stage. The specimens directly lose their bearing capacity after reaching the peak strength. The value of U and U_e increase with the increase of deformation, while the value of U_d remains unchanged (maintains a small value) before reaching the peak stress and increases rapidly exceeding peak strength. These results show that the bonding force between the interfaces under vertical loads is suddenly released during sliding failure. Moreover,

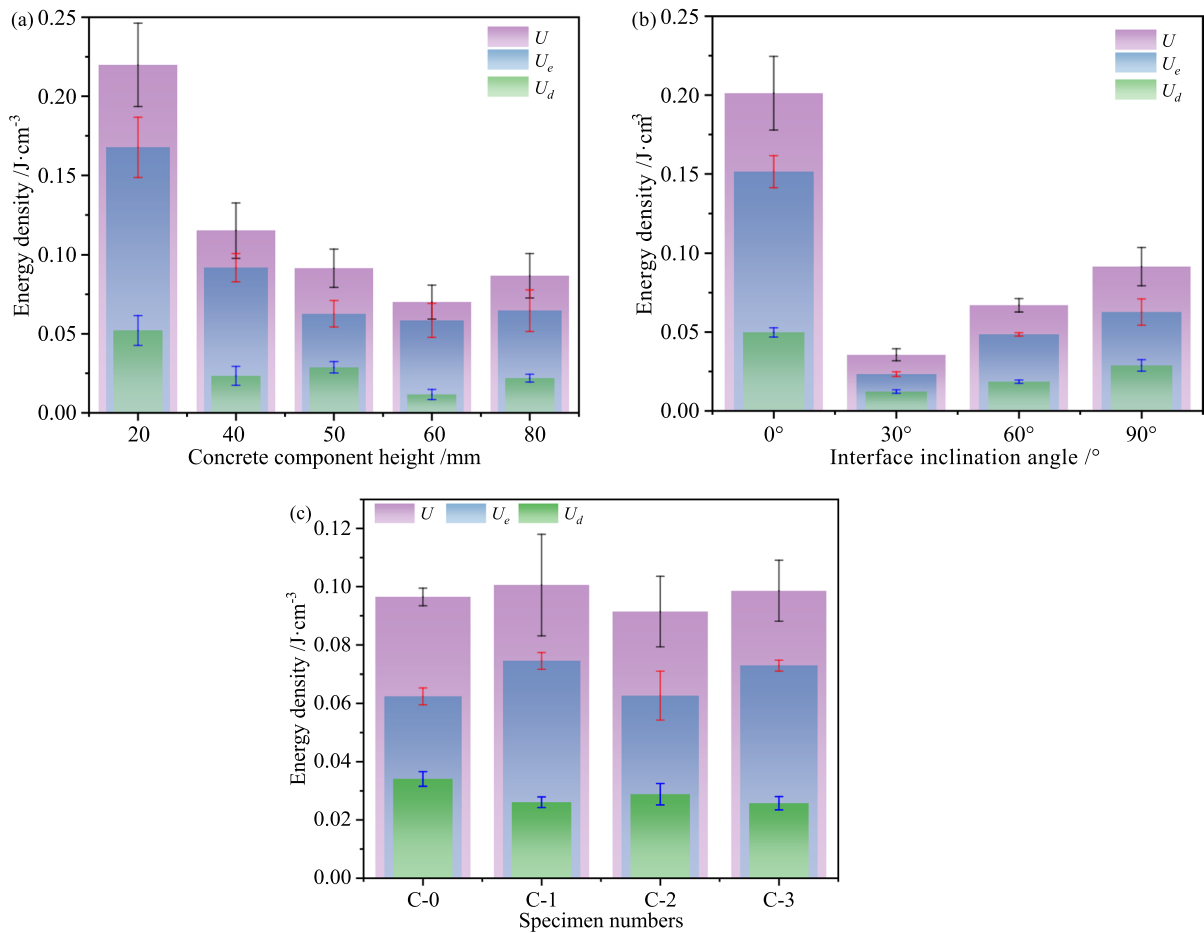


Fig. 12 Energy density at peak stress point **a** concrete component heights **b** interface inclination angles **c** coarse aggregate contents

due to the low interface strength, the total input energy during the entire failure process was lower than that of other interface inclination angle conditions. The deformation and damage process under $\beta = 30^\circ$ is similar to that of horizontally layered rock under direct shear, both of which produce typical shear failure along the weak plane and obtain minimal shear strength (Heng et al. 2015).

3.2.3 Energy at the peak stress point

As shown in Fig. 12a, the value of U and U_e absorbed by CGCSs first decreases with an increase in concrete component height and then remains unchanged, while the concrete component height has few effects on the value of U_d . The granite components with higher strength and more energy need to be absorbed during

the damage process, and the stored elastic energy also increases, leading to larger dissipation energy when damaged. As the concrete component height increases, the input total energy required for damage decreases. When the concrete component height exceeds 50 mm, the failure is mainly concentrated in the concrete component, and the failure degree of the granite component is reduced, leading to the degree of mutual conversion of each energy being the same. The above results indicate that the height of the concrete component influences energy evolution. Moreover, the value of U_e at the peak stress point represents the energy storage limit of the specimen and reflects the ability to resist damage. Hence, due to the presence of granite components with higher strength, the smaller the height of the concrete component, the stronger the ability to resist damage.

Figure 12b displays the energy at the peak stress point for various interface inclination angles. The energy varies "U-shaped" trends, similar to layered rocks' compressive strength anisotropy characteristics (Heng et al. 2015). Under $\beta=0^\circ$, the two components jointly bear the external load, and the damage degree is highest (Fig. 5b). Hence, it needs to absorb larger input energy, and the dissipation energy is higher, which is the most difficult to destroy. Moreover, the dissipation energy required for the failure of $\beta=30^\circ$ is the least, and the failure is easiest. As shown in Fig. 7d, the interface shear failure degree decreases with an increase in interface inclination angle, and the macro failure is formed in the two components. Hence, the value of U and U_d increases when β exceeds 30° .

When $H_c=50$ mm and $\beta=90^\circ$, as shown in Fig. 12c, simultaneous failure of both components is formed for different coarse aggregate contents, leading to similar values of energy density and evolution process at peak stress. This result indicates that the coarse aggregate contents have few effects on the energy conversion process under uniaxial compression load.

3.2.4 Elastic energy consumption ratio

Internal damage and overall failure of CGCSs are essentially part of the conversion process between U_e and U_d . The value of U_d is directly related to the damage and strength of the specimen, and the degree of energy dissipation can reflect the degree of the strength attenuation. Hence, the energy consumption ratio (K) was used to reflect the influence of the combination modes on the energy consumption and energy storage characteristics under different stress stages. K can be expressed by Eq. (9):

$$K = \frac{U_d}{U_e} \quad (9)$$

For ideal elastic materials, the total energy absorbed will be fully converted into elastic energy, and no damage will occur during the deformation, nor will it be consumed in the form of deformation heat production. All the elastic energy is released after unloading, indicating that the values of K is always 0.

However, for heterogeneous materials such as rock or concrete, deformation, micro-crack initiation,

internal friction, and other characteristics will consume energy, eventually reducing strength and forming macroscopic damage. As shown in Sects. 3.1 and 3.2, CGCSs form three failure modes, corresponding to different stress-strain and energy evolution processes. Figure 13 illustrates the value of K and stress-strain under different combination modes. Micro-cracks and pores compaction lead to a high proportion of dissipation energy during the initial loading stage, leading to a quick rise in the value of K . Hence, the value of K is greater than 1.0, which indicates that the specimen is in an unstable state (marked with the red curve) in the compaction stage. Then the degree of compaction decreases with the continuous loading, the value of U_e increases, and the value of U_d decreases, leading to a gradual decrease in the value of K . During the elastic and plastic deformation stage, the energy primarily stored in the form of elastic energy, accompanied by the accumulation of a small number of micro-cracks, and the value of U_d is relatively low. The value of K typically remains between 0 and 1.0, which indicates that the specimen is in a relatively stable state (marked with the blue curve). Moreover, $K = 1.0$ represents the specimen in a critical stable state.

As shown in Fig. 13a, d, the value of K shows a rapid increase after reaching peak stress, indicating that the value of U_d increases sharply, and CGCSs exhibit a typical brittle failure characteristic. The two components are shown in a "parallel" mode under $\beta=0^\circ$, resulting in more significant post-peak brittleness characteristics than $H_c=20$ mm. Particularly, the value of K increases rapidly during the loading process, then decreases gradually, and finally increases sharply after reaching the peak strength (Fig. 13e). No plastic deformation stage directly causes a shear failure along the interface under $\beta=30^\circ$ (Fig. 13e). For $H_c=50$ mm and C-0 specimen (Fig. 13b, c), the value of K did not show a rapidly increasing trend after reaching peak stress, showing a ductile failure characteristic.

3.3 Evolution equation of damage variable

3.3.1 Damage constitutive model

Based on the strain equivalent principle theory, the relationship between "apparent stress" and

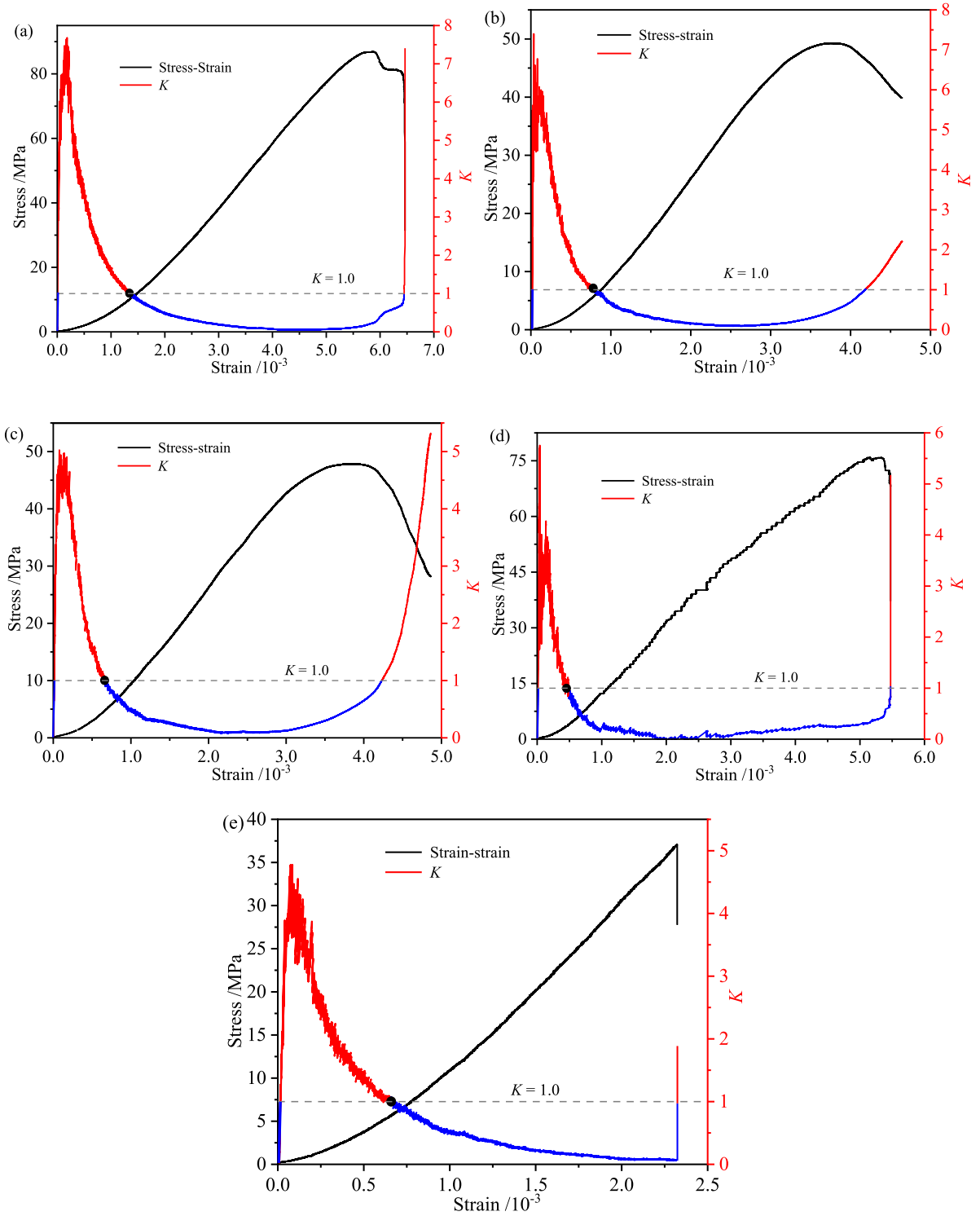


Fig. 13 The elastic energy consumption ratio **a** $H_c = 20$ mm **b** $H_c = 50$ mm ($\beta = 90^\circ$ and C-2) **c** C-0 **d** $\beta = 0^\circ$ **e** $\beta = 30^\circ$

''effective stress'' can be proposed as follows (Lemaitre 1984):

$$[\sigma_i^*] = \frac{[\sigma_i]}{(1 - D_d)} = \frac{[E][\epsilon_i]}{(1 - D_d)} \tag{10}$$

where $[\sigma_i]$ is the apparent stress, $[\sigma_i^*]$ is the effective stress, $[E]$ and $[\epsilon_i]$ is the elastic modulus and strain tensor respectively, D_d is the damage variable.

According to Sect. 3.2, the value of U_d is closely related to the damage and failure process of CGCSs. Therefore, assuming that the damage is continuously developed and is the gradual accumulation of failure in mesoscopic elements. The damage probability of the mesoscopic elements is related to U_d and follows the Weibull distribution function. The probability density function can be expressed as (Shen et al. 2024; Jiang et al. 2022):

$$P(U_d) = \begin{cases} \frac{m}{F_0} \left(\frac{U_d}{F_0}\right)^{m-1} \exp\left[-\left(\frac{U_d}{F_0}\right)^m\right], & F > 0 \\ 0, & F \leq 0 \end{cases} \tag{11}$$

where U_d is the elemental dissipation energy. m and F_0 are the Weibull parameters, m is the brittleness of rock and F_0 is the macroscopic average strength of rock.

The energy consumed during the failure process is proportional to the number of damaged mesoscopic elements. The damage variable D_d can be calculated (Shen et al. 2024; Jiang et al. 2022):

$$D_d = \frac{N_d}{N} \tag{12}$$

where N_d and N represent the numbers of damaged mesoscopic elements and the total number of mesoscopic elements, respectively.

When U_d increases to $U_d + dU_d$, the number of damaged mesoscopic elements increases by $NP(U_d)dU_d$. If the external load leads to the dissipation energy increases from 0 to U_d , the total number of damaged mesoscopic elements is (Zhang et al. 2021a, b):

$$N_d(U_d) = \int_0^{U_d} NP(U_d)dU_d = N \left\{ 1 - \exp\left[-\left(\frac{U_d}{F_0}\right)^m\right] \right\} \tag{13}$$

Substituting Eq. (13) into Eq. (12) yields:

$$D_d = 1 - \exp\left[-\left(\frac{U_d}{F_0}\right)^m\right] \tag{14}$$

According to the generalized Hooke's law, the damage constitutive model based on energy dissipation can be expressed as:

$$\sigma = E\epsilon \left\{ \exp\left[-\left(\frac{U_d}{F_0}\right)^m\right] \right\} \tag{15}$$

The stress-strain fitting curve obtained from Eq. (15) is approximately straight or convex in shape under lower stress level conditions, which is suitable for characterizing the dense rock with no obvious compaction stage (Zhang et al. 2021a, b). However, the failure is mainly caused by the concrete components, there are obvious compaction stages (lower convex shape) at lower stress level conditions. Hence, to accurately characterize the whole damage process of CGCSs, the compaction stage is considered to be calculated separately. Deng et al. (2017) indicated that the stress-strain curve shape was mainly determined by the $\exp(-(U_d/F_0)^m)$ term in Eq. (15). This term is changed to $1 - \exp(-(U_d/F_0)^m)$ to represent the low convex shape characteristic of the stress-strain in the compaction stage. The stress-strain after the compaction stage continues to adopt the form of Eq. (15). Therefore, the damaged constitutive model can be expressed as:

$$\begin{cases} \sigma = E\epsilon_A \left\{ 1 - \exp\left[-\left(\frac{U_{dA}}{F_{01}}\right)^{m_1}\right] \right\}, & \epsilon \leq \epsilon_A \\ \sigma = E(\epsilon - \epsilon_A) \exp\left[-\left(\frac{U_d - U_{dA}}{F_{02}}\right)^{m_2}\right] + \sigma_A, & \epsilon > \epsilon_A \end{cases} \tag{16}$$

where σ_A , ϵ_A , and U_{dA} are the stress, strain, and dissipation energy at the end point of compaction stage, respectively.

3.3.2 Determination of the value of m and F_0

The key point to establishing the constitutive models lies in determining Weibull parameters. There are two methods to solve the statistical model in Eq. (15). The first method is to solve the equation directly, which has strict mathematical and physical significance but is complicated. The second is the data fitting method. Although it cannot strictly meet the solution conditions,

it has a simple process, and the fitting effect is good. Therefore, considering the characteristics of these two methods, the data fitting method for the compaction stage and the solution equation method for the post-compaction stage were used in this study.

(1) Data fitting method

When $\epsilon \leq \epsilon_A$, Eq. (16) is deformed and logarithmically calculated twice, which can be expressed as:

$$\ln\left[-\ln\left(1 - \frac{\sigma}{E\epsilon}\right)\right] = m_1 \ln(U_d) - m \ln(F_{01}) \tag{17}$$

Making $y = \ln\left[-\ln\left(1 - \frac{\sigma}{E\epsilon}\right)\right]$, $x = \ln(U_d)$, and $b = -m_1 \ln(F_0)$, Eq. (17) can be expressed as:

$$y = m_1 x + b \tag{18}$$

The value of m_1 and b can be calculated by fitting the results in the compaction stage using data fitting, and then $F_{01} = \exp(-b/m_1)$.

(2) Solution equation method

When $\epsilon > \epsilon_A$, the value of m_2 and F_{02} can be determined by considering the peak stress condition and geometric condition of the stress–strain curve, which can be expressed as:

$$\begin{cases} \sigma|_{\epsilon=\epsilon_c} = \sigma_c \\ \frac{d\sigma}{d\epsilon}|_{\epsilon=\epsilon_c} = 0 \end{cases} \tag{19}$$

where σ_c and ϵ_c are the stress and strain at peak point, respectively.

Substituting Eqs. (16) and (19), the value of m_2 and F_{02} after the compaction stage can be expressed as:

$$\begin{cases} m_2 = \frac{U_{dA} - U_d}{(\epsilon_c - \epsilon_A)(\sigma_c - \sigma_A) \ln\left[\frac{\sigma_c - \sigma_A}{E(\epsilon_c - \epsilon_A)}\right]} \\ F_{02} = \sqrt[m_2]{n(\epsilon_c - \epsilon_A)(\sigma_c - \sigma_A)(U_d - U_{dA})^{m_2 - 1}} \end{cases} \tag{20}$$

3.3.3 Verification of the damage constitutive model

According to Sects. 3.2.2 and 3.2.4, the dissipation energy is greater than elastic energy due to the micro-failure in the compaction stage. The elastic energy accumulates, and the dissipation energy is mainly unchanged in the elastic stage. Moreover, the value of K can effectively reflect the energy evolution characteristics, which can well reflect the deformation and failure of CGCSs under uniaxial compression. Therefore, the black dot mark on the curve of K value ($K=1.0$) in Fig. 13 is a dividing point between the compaction and elastic stages. This point corresponds to a specific strain value, defined as ϵ_A . Based on Sect. 3.3.2, the value of m and F_0 under different loading stages can be determined, as shown in Table 4.

Figure 14 compares experimental and theoretical values under different combination modes. During

Table 4 Weibull parameters under different combination modes

| Specimens | | Compaction stage ($\epsilon \leq \epsilon_A$) | | Non-compaction stage ($\epsilon > \epsilon_A$) | |
|-------------------------------|-----|---|----------|--|----------|
| | | m_1 | F_{01} | m_2 | F_{02} |
| Concrete component height /mm | 20 | 0.0231 | 0.4628 | 0.3220 | 0.8459 |
| | 40 | 0.0093 | 0.4785 | 0.2132 | 0.7556 |
| | 50 | 0.3932 | 0.0058 | 0.1440 | 0.7826 |
| | 60 | 0.0039 | 0.6095 | 0.1503 | 0.7228 |
| | 80 | 0.0022 | 0.6371 | 0.1437 | 0.8759 |
| Interface inclination angle | 0° | 0.0048 | 0.3255 | 0.4320 | 0.6020 |
| | 30° | 0.0075 | 0.2852 | 2.6990 | 0.3270 |
| | 60° | 0.0159 | 0.1245 | 0.2956 | 0.5665 |
| | 90° | 0.3932 | 0.0058 | 0.1440 | 0.7826 |
| Coarse aggregate contents | C-0 | 0.0028 | 0.4695 | 0.1510 | 0.7745 |
| | C-1 | 0.0070 | 0.3367 | 0.1904 | 0.7290 |
| | C-2 | 0.3932 | 0.0058 | 0.1440 | 0.7826 |
| | C-3 | 0.0232 | 0.4136 | 0.9470 | 1.1062 |

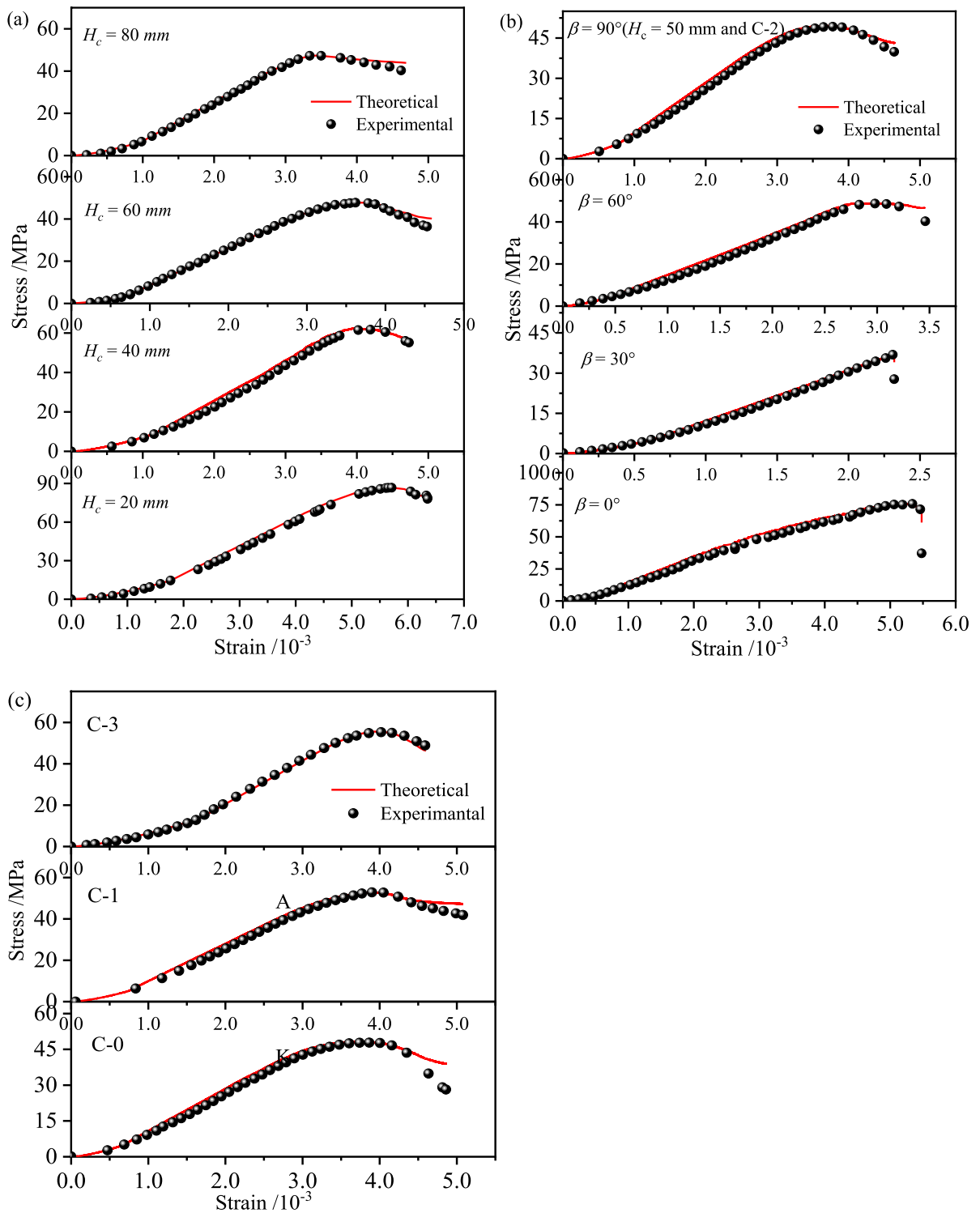


Fig. 14 Experimental and theoretical stress–strain curves of CGCSs **a** concrete component heights **b** interface inclination angles **c** coarse aggregate contents

the pre-peak stage, including the compaction stage, linear elastic deformation stage, and plastic deformation stage, the total stress–strain curves show a high consist in the experimental curves. The theoretical value of peak stress is also the same as the test. For the post-peak stage, it can also better reflect the characteristics of the sharp decline of stress and also has strong applicability to ductile failure. These results indicate that the piecewise damage constitutive model proposed in this study is reasonable and can more accurately characterize the deformation and failure characteristics of CGCSs under uniaxial compression.

These results further indicate that the nonlinear characteristics of the compaction stage must be considered in the damage constitutive analysis of CGCSs.

3.3.4 Parameter-sensitive analysis

To investigate the influence of m on the stress and deformation characteristic and determine its physical significance, taking $\beta=90^\circ$ as an example, the value of F_0 remains unchanged, and the value of m is changed to fit Eq. (16). It is worth noting that the

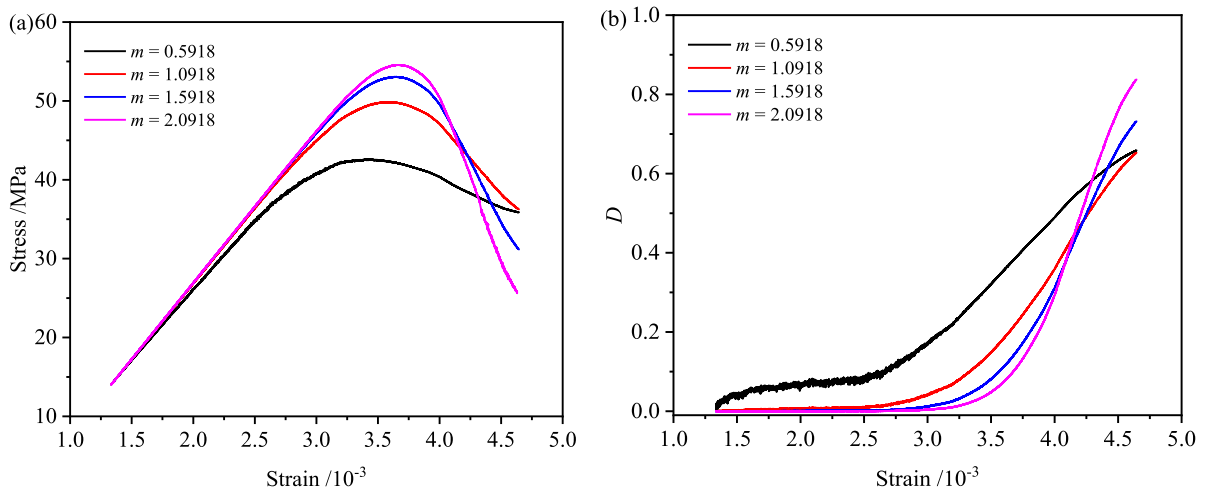


Fig. 15 Sensitivity analysis of the Weibull distribution parameters m **a** stress–strain **b** D

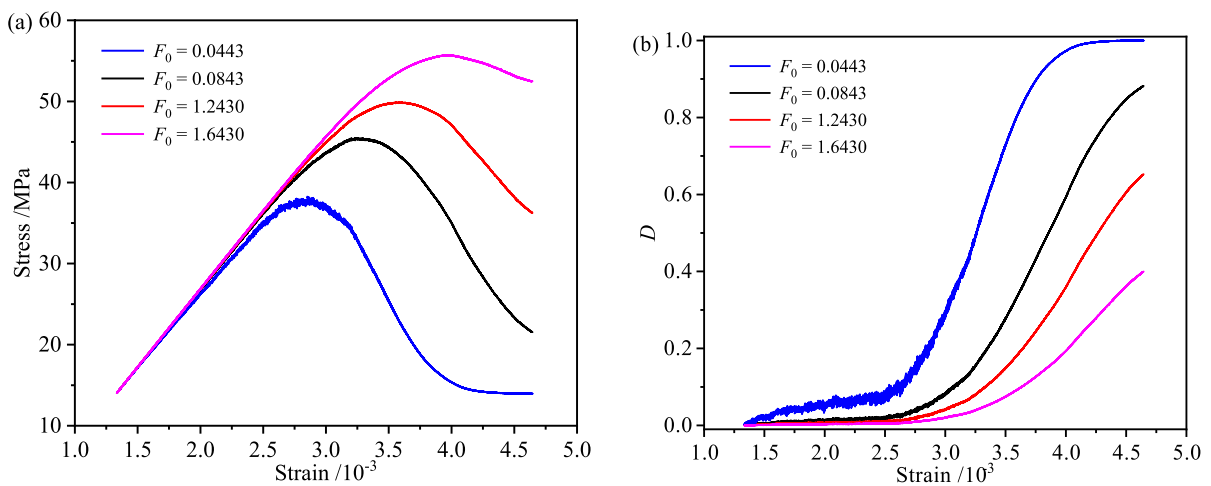


Fig. 16 Sensitivity analysis of the Weibull distribution parameters F_0 **a** stress–strain **b** D

sensitivity analysis of Weibull distribution parameters is only for deformation after the compaction stage.

As shown in Fig. 15a, the value of m significantly influences the plastic deformation stage. With the increase of parameter m , the degree of plastic deformation decreases, and the strain hardening degree and the peak strength increase. Moreover, the stress–strain curve’s post-peak section becomes steeper with parameter m increases. This can be explained as the physical significance of parameter m represents the concentration of the strength distribution of the micro-elements inside the specimens, and its value reflects the material brittleness (Jiang et al. 2022). The microelement strength of the specimens is more concentrated at the peak under a larger value of parameters m , resulting in an obvious post-peak stress drop phenomenon, and then showing more significant brittle failure characteristics. It can be observed from Fig. 15b that the strain value corresponding to the damage accumulation began to increase with parameter m increases, and the damage accumulation rate was also increased.

Figure 16 shows the influence of F_0 on the deformation and damage characteristics. It can be seen that parameter F_0 has few influences on the overall shape of the stress–strain curve. The same deformation rate is observed during the elastic stage, but the

peak strength and strain increase gradually with an increase in F_0 . Therefore, the physical significance of parameter F_0 can be expressed as an indicator of the macroscopic strength of the specimens (Jiang et al. 2022). From Fig. 16b, the strain value corresponding to the damage accumulation of the specimen began to increase with parameter m increases, while the damage accumulation rate decreased.

4 Stress analysis

4.1 Concrete component heights

Due to the difference in mechanical properties between the two components and the existence of an interface, the mechanical properties of CGCSs are significantly different from that of the concrete and granite single specimens. The discontinuity and anisotropy of the composite specimen structure cause the discontinuity and non-uniformity of its internal stress distribution, leading to complex mechanical properties. By summarizing the mechanical parameters and failure modes of CGCSs, it is observed that the failure mechanism results from the comprehensive interaction of the two components and the interface. To

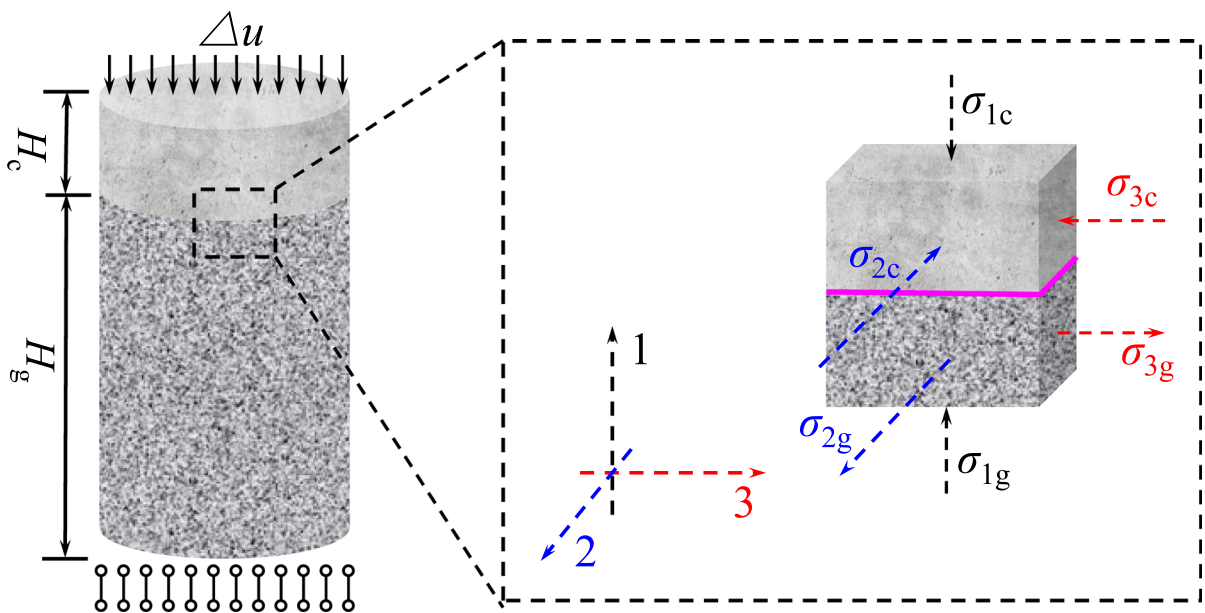


Fig. 17 Stress state of CGCSs under different concrete component heights

further understand the failure mechanism of CGCSs under uniaxial compression load, we studied the stress state characteristics for different combination modes.

Figure 17 shows the stress state near the interface under different concrete component heights. Due to the significant differences in the elastic modulus and Poisson's ratio of concrete and granite materials, the radial strain of those components mutually constrains each other under external load, leading to a mutual restraint effect near the interface. For the concrete and granite components on either side of the interface, the constraint stress is equal in magnitude but opposite in direction. This results in tensile (compressive) in one component and compressive (tensile) stress in the other component.

The elastic modulus of concrete with a mixture of 1:0.38:1.11:2.72 is 18.87 GPa, while the granite is 22.73 GPa. Hence, under compression loading conditions, the radial strain of the granite component is lower than that of the concrete component. According to the deformation coordination principle, the radial deformation of concrete components is limited by granite components, while concrete components promote the radial deformation of granite components. Under this interaction, radial compressive stress occurs near the interface's concrete component. In contrast, radial tensile stress occurs in the granite component near the interface, as shown in Fig. 17. Moreover, due to the radial strain constraints, no shear stress occurs at the interface when $\beta=90^\circ$. Therefore, near the interface, it changes from a unidirectional compressive stress state to a triaxial stress state. In this triaxial state, the concrete component experiences compressive stress, and the granite component experiences compressive and tensile stress. The concrete and granite components outside the interface region remain in a unidirectional compressive stress state.

It can be seen that the concrete component near the interface changes from a unidirectional compressive stress state to a triaxial compressive stress state, resulting in an increased axial ultimate compressive strength compared to the concrete component outside the interface region. Conversely, the granite component experiences horizontal tensile stress, reducing its axial ultimate compressive strength relative to the granite component outside

the interface region. However, because the granite's strength (116.52 MPa) is much greater than that of concrete (46.66 MPa), the strength of the granite component near the interface remains higher than that of the concrete component. The change in the strength of each part affects the failure sequence in CGCSs. Failure first occurs in the concrete component far away from the interface and gradually develops towards the interface. When the failure energy is sufficient, the granite components fail. Due to the lower strength of the concrete component, increasing the value of H_c results in damage concentrating in the concrete components and consuming significant energy, while the granite components remain minimally or with no damage. This failure pattern indicates that the weaker components determined the value of σ_{CGCS} . Additionally, as the value of H_c increases, the influence of concrete components on the value of σ_{CGCS} enhances, while the granite component's influence diminishes. Hence, the value of σ_{CGCS} is negatively correlated with H_c . These theoretical results are consistent with the experimental results in this study. Moreover, when the strength of the concrete and granite is closer (such as high-strength concrete materials), further studies will be needed to elucidate the mechanical response of these combination modes.

4.2 Interface inclination angle

Figure 18 shows the stress state near the interface under various interface inclination angles. The bonding strength of the interface is weak in CGCSs. Shearing stress forms near the interface, leading to shear failure during the initial loading stage and separating the two components into independent entities. Therefore, as the loading continues to increase, the two components remain in a unidirectional compressive stress state, and the axial and radial deformation of the two components do not affect each other, as shown in Fig. 18a. Subsequently, macroscopic damage gradually forms in the weaker concrete component. Meanwhile, the granite component continues to bear part of the external load until its ultimate strength is reached, leading to the overall instability failure of the CGCSs. This failure sequence is the primary reason for the maximum value of σ_{CGCS} under $\beta=0^\circ$.

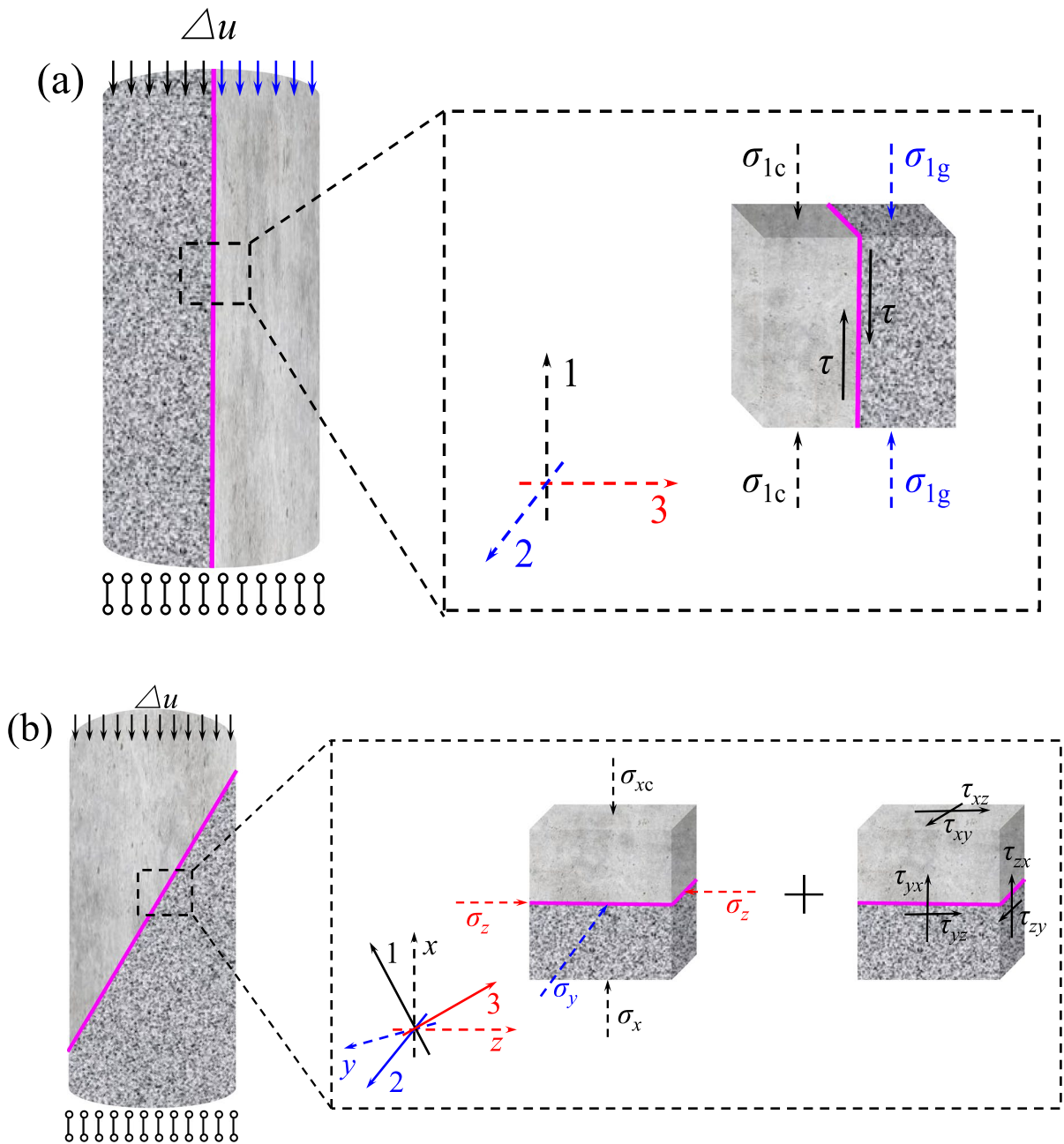


Fig. 18 Stress state of CGCSs **a** $\beta=0^\circ$ **b** $\beta=30^\circ$

Due to the difference in mechanical parameters (strength and deformation) of the two components and the existence of an inclined interface, the stress state is more complicated than $\beta=90^\circ$ (as shown in Fig. 17). The following conclusions can be drawn

from the stress state analysis under $\beta=30^\circ$, as shown in Fig. 18b.

- (1) The uncoordinated deformation of the two components near the interface leads to a mutual

restraint effect at this location, resulting in a complex triaxial stress state in CGCSs. Due to the inclined interface, both normal and shear stress occur near the interface. However, the concrete and granite components outside the interface region remain in a unidirectional compressive stress state.

- (2) For the CGCSs with an inclined interface, the value of σ_{CGCS} primarily determined by concrete and granite components and the interface and is closely related to the value of β . As shown in Figs. 5b and 18b, the shear stress leads to shear failure along the interface more easily, and the value of σ_{CGCS} depends on the bonding strength of the interface, resulting in minimal strength being obtained at $\beta=30^\circ$. As the value of β increases, CGCSs gradually change to a "series" mode, reducing the shear stress near the interface and the probability of shear failure along the interface. Damage mainly forms in the concrete component, leading to an increase in σ_{CGCS} , with values similar to the strength of concrete specimens. These results theoretically explain the mechanical properties and failure characteristics of CGCSs for various interface inclination angles.
- (3) The stress, strain, and strength near the interface are closely related to the two components' elastic modulus, Poisson's ratio, and shear modulus. Theoretically, the more significant the difference in elastic modulus and Poisson's ratio between the two components, the more pronounced the mutual restraint effect forms near the interface, leading to significant changes in the mechanical properties within the CGCSs.

It is worth noting that for different combination modes under uniaxial compression, the difference in the mechanical properties of the two components changes the stress state in CGCSs, especially near the interface. This change results in the mechanical and failure characteristics of CGCSs being different from those of individual specimens. The value of σ_{CGCS} and failure modes are primarily determined by concrete, granite, and interface properties. Therefore, to ensure the safety and stability of concrete–rock composite structures, it is necessary to consider the comprehensive influence of the combination modes

and loading conditions. The conclusions of this study provide important support for understanding the mechanics, energy, and failure evolution mechanisms of CGCSs under uniaxial compression from theoretical and experimental perspectives.

5 Conclusions

This study investigates mechanical and failure characteristics, energy evolution process, and damage constitutive model of CGCSs for different combination modes under uniaxial compression. The main conclusions are as follows:

- (1) The concrete component failure and the shear failure along the interface are formed at $H_c=80$ mm and $\beta=30^\circ$, respectively. The simultaneous failure of both components occurs in other combination modes. The fractal dimension D_f is positively correlated with H_c and coarse aggregate contents, "U-shaped" variation trends are observed under different β .
- (2) The compressive strength is negatively correlated with H_c , while it shows "U-shaped" trends when β changes from 0° to 90° . Meanwhile, under the synthetical effect of coarse aggregate shape, distribution, and contents, the overall trend of compressive strength increases with an increase in coarse aggregate contents. The stiffness is negatively correlated with H_c and β , while it is positively correlated with the coarse aggregate contents. The variation amplitude of stiffness is not evident under different combination modes.
- (3) The stress–strain and energy evolution curves can be divided into four stages. The typical brittle failure characteristics occur at $\beta=0^\circ$, $\beta=30^\circ$, and $H_c=20$ mm, while the ductile failure characteristics are observed in other combination modes. The value of K first increases and then decreases to maintain a lower value and rises again near the peak strain, which can well reflect the deformation and failure characteristics of CGCSs under uniaxial compression.
- (4) A piecewise damage constitutive model is proposed to characterize the damage evolution law for different combination modes under uniaxial compression. The theoretically calculated values are well consistent with the experimental data,

which verifies the validity and reasonableness of this damage constitutive model.

It is important to note that the effects of complex loading conditions (triaxial and dynamic loads) and environment conditions (e.g., high temperature, humidity variation, and freeze–thaw cycles) on the mechanical response of CGCSs require further investigation. Additionally, in future studies, the adaptability of the proposed piecewise damage constitutive model should be validated through numerical simulation, and a systematic sensitivity analysis should also be conducted to explore the influence of complex loads and combination modes on the model parameters.

Author contributions ZD: Investigation, Formal analysis, Funding acquisition, Writing-original draft; YL: Investigation, Formal analysis, Writing-original draft; BG: Conceptualization, Methodology, Supervision, Writing-review and editing; RY: Formal analysis, Validation; ZL: Formal analysis, Visualization, Writing-review and editing; SW: Supervision, Project administration, Writing-review and editing; CT: Resources, Writing-review and editing.

Funding This work was funded by the National Natural Science Foundation of China (No. 52104084), the Henan Provincial Science and Technology Research Project (No. 232102321128), and the Program for Innovative Research Team (in Science and Technology) in University of Henan Province (No. 22IRTSTHN005).

Availability of data and materials The data underpinning this publication can be accessed from Brunel University London's data repository (Brunelfigshare) under a CCBY license using the DOI of 10.17633/rd.brunel.27939117.

Declarations

Competing interests The authors declare that they have no known competing financial interests or personal relationships that could have appeared to influence the work reported in this paper.

Open Access This article is licensed under a Creative Commons Attribution 4.0 International License, which permits use, sharing, adaptation, distribution and reproduction in any medium or format, as long as you give appropriate credit to the original author(s) and the source, provide a link to the Creative Commons licence, and indicate if changes were made. The images or other third party material in this article are included in the article's Creative Commons licence, unless indicated otherwise in a credit line to the material. If material is not included in the article's Creative Commons licence and your intended use is not permitted by statutory regulation or exceeds the permitted use, you will need to obtain permission directly

from the copyright holder. To view a copy of this licence, visit <http://creativecommons.org/licenses/by/4.0/>.

References

- Chang X, Guo TF, Zhang S (2020) Cracking behaviours of layered specimen with an interface crack in Brazilian tests. *Eng Fract Mech* 228:106904. <https://doi.org/10.1016/j.engfracmech.2020.106904>
- Cui T, He HX, Yan WM, Zhou DX (2020) Compression damage constitutive model of hybrid fiber reinforced concrete and its experimental verification. *Constr Build Mater* 264:120026. <https://doi.org/10.1016/j.conbuildmat.2020.120026>
- Deng HF, Hu AL, Li JL, Zhang XJ, Hu Y, Chang DL, Zhu M (2017) Statistical damage constitutive model of sandstone under water-rock interaction. *Rock Soil Mech* 38(3):631–639. <https://doi.org/10.16285/j.rsm.2017.03.003>
- Du XH, Xue JH, Shi Y, Cao CR, Shu CM, Li KH, Ma Q, Zhan KL, Chen ZH, Wang SL (2023) Triaxial mechanical behaviour and energy conversion characteristics of deep coal bodies under confining pressure. *Energy* 26:126443. <https://doi.org/10.1016/j.energy.2022.126443>
- Feng Q, Xu JS, Cai CG, Liu WW, Jin JC, Han WW, Qin Z (2024) Damage constitutive model and meso-failure characteristics of freeze-thaw rock under triaxial compression. *B Eng Geol Environ* 83(4):112. <https://doi.org/10.1007/s10064-024-03594-0>
- Gao ZL, Liu ZB, Tian F, Shen WQ (2022) Strength, energy evolution and cracking process of sandstone under high-temperature and high-pressure coupled true triaxial compression. *Geomech Geophys Geo-Energy Geo-Resour* 8(6):176. <https://doi.org/10.1007/s40948-022-00490-3>
- Gong FQ, Shi RH, Xu L (2022) Linear energy storage and dissipation laws of concrete under uniaxial compression at different ages. *Constr Build Mater* 318:125963. <https://doi.org/10.1016/j.conbuildmat.2021.125963>
- Gong HL, Luo Y, Wei XQ, Peng JJ, Li XP (2023) Investigations on dynamic failure behaviors and energy transfer efficiency of heat-treated high-performance concrete under multiaxial constraints. *Constr Build Mater* 409:133930. <https://doi.org/10.1016/j.conbuildmat.2023.133930>
- Gu XL, Hong L, Wang ZL, Lin F (2013) Experimental study and application of mechanical properties for the interface between cobblestone aggregate and mortar in concrete. *Constr Build Mater* 46:156–166. <https://doi.org/10.1016/j.conbuildmat.2013.04.028>
- Gutiérrez-Ch JG, Senent S, Melentijevic S, Jimenez R (2018) Distinct element method simulations of rock–concrete interfaces under different boundary conditions. *Eng Geol* 240:123–139. <https://doi.org/10.1016/j.enggeo.2018.04.017>
- Heng S, Yang CH, Zhang BP, Guo YT, Wang L, Wei TL (2015) Experimental research on anisotropic properties of

- shale. *Rock Soil Mech* 36(3):609–616. <https://doi.org/10.16285/j.rsm.2015.03.001>
- Jiang J, Hou ZM, Hou KP, Lu YF, Sun HF, Niu XD (2022) The damage constitutive model of sandstone under water–rock coupling. *Geofluids*. <https://doi.org/10.1155/2022/1731254>
- Lambert C, Buzzi O, Giacomini A (2010) Influence of calcium leaching on the mechanical behavior of a rock–mortar interface: a DEM analysis. *Comput Geotech* 37:258–266. <https://doi.org/10.1016/j.compgeo.2009.09.006>
- Li XJ, Zhang JG, Chen XD, Lv MY, Li KJ (2022a) Research on direct tensile experiment of rock–concrete interface using acoustic emission technology. *Russ J Nondestruct* 57(12):1082–1095. <https://doi.org/10.1134/S106183092112010X>
- Li XJ, Lan LJ, Zhang JG, Tang JH, Lv MY, Liu CZ, Han XR (2022b) A new method for measuring the adhesion strength of rock–concrete specimens based on the calibration interface of the modified flat-joint model. *Eng Fail Anal* 142:106752. <https://doi.org/10.1016/j.engfailanal.2022.106752>
- Li YL, Guo HY, Zhou H, Li Y, Chen JH (2022c) Damage characteristics and constitutive model of concrete under uniaxial compression after freeze–thaw damage. *Constr Build Mater* 345:128171. <https://doi.org/10.1016/j.conbuildmat.2022.128171>
- Liu J, Yu WX, Li D, Du XL (2021) Numerical and theoretical investigation on the size effect of concrete compressive strength considering the maximum aggregate size. *Int J Mech Sci* 192:106130. <https://doi.org/10.1016/j.ijmecsci.2020.106130>
- Liu XJ, Zhuang DL, Xiong J, Zhou YS, Liu JJ, Deng C, Liang LX, Ding Y, Jian XM (2024) Anisotropy and energy evolution characteristics of shales: a case study of the Longmaxi Formation in Southern Sichuan Basin, China. *Geofluids*. <https://doi.org/10.1155/2024/4186113>
- Lu JY, Zhou ZL, Chen XQ, Wang PY, Rui YC, Cai X (2022) Experimental investigation on mode I fracture characteristics of rock–concrete interface at different ages. *Constr Build Mater* 349:128735. <https://doi.org/10.1016/j.conbuildmat.2022.128735>
- Luan JJ, Chen XD, Ji T, Bai Y, Yu X (2024) Mechanical behavior and energy dissipation of sandstone–shotcrete under monotonic and cyclic triaxial loading. *Int J Geomech* 24(4):04024028. <https://doi.org/10.1061/IJG-NAI.GMENG-8901>
- Lemaitre J (1984) How to use damage mechanics. *Nucl Eng Des* 80(2):233–245. [https://doi.org/10.1016/0029-5493\(84\)90169-9](https://doi.org/10.1016/0029-5493(84)90169-9)
- Luo Y, Gong HL, Xu K, Pei CH, Wei XQ, Li XP (2022) Progressive failure characteristics and energy accumulation of granite with a pre-fabricated fracture during conventional triaxial loading. *Theor Appl Fract Mech* 118:103219. <https://doi.org/10.1016/j.tafmec.2021.103219>
- Pereira R, Batista AL, Neves LC, Lemos JV (2022) Deduction of ultimate equilibrium limit states for concrete gravity dams keyed into rock mass foundations based on large displacement analysis. *Structures* 38:1180–1190. <https://doi.org/10.1016/j.istruc.2022.02.049>
- Qin H, Cao S, Yilmaz E (2024) Mechanical, energy evolution, damage and microstructural behavior of cemented tailings–rock fill considering rock content and size effects. *Constr Build Mater* 411:134449. <https://doi.org/10.1016/j.conbuildmat.2023.134449>
- Saichi T, Bouaanani N (2024) Contribution of 3D roughness along concrete–rock interface to the sliding stability of concrete gravity dams. *Geotech Geol Eng*. <https://doi.org/10.1007/s10706-024-02758-9>
- Selçuk L, Aşma D (2019) Experimental investigation of the rock–concrete bi materials influence of inclined interface on strength and failure behavior. *Int J Rock Mech Min* 123:104119. <https://doi.org/10.1016/j.ijrmmms.2019.104119>
- Shen MX, Bi J, Zhao Y, Wang CL, Wei T, Du B (2022) Study on the mechanical characteristics and damage evaluation of concrete–rock combination after high temperatures exposure. *Constr Build Mater* 330:127278. <https://doi.org/10.1016/j.conbuildmat.2022.127278>
- Shen MX, Zhao Y, Bi J, Wang CL, Du B (2024) Microstructure evolution and damage mechanisms of concrete–rock-composite corrosion in acid environment. *J Build Eng* 82:108336. <https://doi.org/10.1016/j.jobe.2023.108336>
- Son M (2013) Adhesion strength at the shotcrete–rock concrete in rock tunneling. *Rock Mech Rock Eng* 46:1237–1246. <https://doi.org/10.1007/s00603-013-0380-0>
- Solecki R, Conant RJ (2003) *Advanced mechanics of materials*. Oxford University Press, London
- Specification for mix proportion design of ordinary concrete: JGJ 55–2011 (2011). China Architecture & Building Press, Beijing
- Wang L, Wang LQ, Yang Y, Zhu X, Zhang D, Gao XC (2022) Discrete element modeling of rock–concrete bi-material discs under dynamic tensile loading. *Constr Build Mater* 327:126962. <https://doi.org/10.1016/j.conbuildmat.2022.126962>
- Xiao CL, Yang RS, Ma XM, Wang YB, Ding CX (2024) Damage evaluation of rock blasting based on multi-fractal study. *Inter J Impact Eng* 188:104953. <https://doi.org/10.1016/j.ijimpeng.2024.104953>
- Yang LY, Zhang F, Lin CY, Xie HZ, Fan P (2022) Experimental study on failure characteristics of rock–fiber concrete composite under compression load. *Structures* 44:1863–1873. <https://doi.org/10.1016/j.istruc.2022.09.007>
- Yang KX, Hu Q, Zhao H, Zhao MH, Zhou S (2023) Numerical study on the shear behavior of concrete–rock joints with similar triangular asperities. *Comput Geotech* 159:105468. <https://doi.org/10.1016/j.compgeo.2023.105468>
- Yang LJ, Hou C, Zhu WC, Li L (2024) Effect of roughness on shear behavior of interface between cemented paste backfill and rock. *Constr Build Mater* 411:134312. <https://doi.org/10.1016/j.conbuildmat.2023.134312>
- Yuan SS, Du B, Shen MX (2024a) Experimental and numerical investigation of the mechanical properties and energy evolution of sandstone–concrete combined body. *Sci Rep-UK* 14(1):1–20. <https://doi.org/10.1038/s41598-024-53959-4>
- Yuan WY, Dong W, Zhang BS, Yu DH (2024b) Determination of SIFs and application of a SIF-based fracture criterion for concrete–rock interface under sustained loading. *Cem Concr Compos* 145:105342. <https://doi.org/10.1016/j.cemconcomp.2023.105342>

- Yu WX, Xie CX, Liu J, Du XL (2024) Effects of fiber characteristics and specimen sizes on static and dynamic split-tensile failures of BFLAC: 3D mesoscopic simulations. *Eng Fract Mech* 295:109759. <https://doi.org/10.1016/j.engfracmech.2023.109759>
- Zhao H, Zhou S, Zhao MH (2019) Load transfer in drilled piles for concrete–rock interface with similar triangular asperities. *Int J Rock Mech Min* 120:58–67. <https://doi.org/10.1016/j.ijrmms.2019.06.003>
- Zhao Y, Shen MX, Bi J, Wang CL, Yang YT, Du B, Ning L (2022) Experimental study on physical and mechanical characteristics of rock–concrete combined body under complex stress conditions. *Constr Build Mater* 324:126647. <https://doi.org/10.1016/j.conbuildmat.2022.126647>
- Zhao TD, Li Q, Yu BB, Huang C, Gao ZH, Wang K (2023) Experimental study on dynamic mechanical properties of mortar-sandstone composite under impact load. *Structures* 51:1061–1070. <https://doi.org/10.1016/j.istruc.2023.03.086>
- Zhang LL, Cheng H, Wang XJ, Liu JM, Guo LH (2021a) Statistical damage constitutive model for high-strength concrete based on dissipation energy density. *Crystals* 11(7):800. <https://doi.org/10.3390/cryst11070800>
- Zhang R, Li BB, Xu J, Gao Z, Chen S, Wang B (2021b) Study on triaxial compression damage evolution characteristics of coal based on energy dissipation. *Chin J Rock Mech Eng* 40(8):1614–1627. <https://doi.org/10.13722/j.cnki.jrme.2020.1133>
- Zhang YC, Huang M, Jiang YJ, Wang Z (2023) Mechanics, damage and energy degradation of rock–concrete interfaces exposed to high temperature during cyclic shear. *Constr Build Mater* 405:133229. <https://doi.org/10.1016/j.conbuildmat.2023.133229>
- Zhang XQ, Gong HL, Luo Y, Peng JJ, Li QL, Yang CN (2024) Characterization and constitutive modeling of the high strain rate behavior of granite at low temperatures. *Mech Time Depend Mat*. <https://doi.org/10.1007/s11043-024-09667-7>
- Zheng MH, Liang YP, Staat M, Li QG, Li JB (2024) Discontinuous fracture behaviors and constitutive model of sandstone specimens containing non-parallel prefabricated fissures under uniaxial compression. *Theor Appl Fract Mech* 131:104373. <https://doi.org/10.1016/j.tafmec.2024.104373>
- Zhou ZL, Lu JY, Cai X (2020) Static and dynamic tensile behavior of rock–concrete bi-material disc with different interface inclinations. *Constr Build Mater* 256:119424. <https://doi.org/10.1016/j.conbuildmat.2020.119424>
- Zhou ZL, Lu JY, Cai X, Rui YC, Tan LH (2022) Water saturation effects on mechanical performances and failure characteristics of rock–concrete disc with different interface dip angles. *Constr Build Mater* 324:126684. <https://doi.org/10.1016/j.conbuildmat.2022.126684>

Publisher's Note Springer Nature remains neutral with regard to jurisdictional claims in published maps and institutional affiliations.